A Trailing-Edge Noise Model for Serrated Edges

Benshuai Lyu [*]

Department of Engineering, University of Cambridge

Mahdi Azarpeyvand [†]

Department of Mechanical Engineering, University of Bristol

Samuel Sinayoko [‡]

Institute of Sound and Vibration Research, University of Southampton

This paper is concerned with the development of a theoretical model for the prediction of the sound radiated by serrated trailing-edges. The proposed model is based on Fourier expansion and Amiet's formulation. By using an iterative PDE-solving procedure, the scattered pressure field on the surface of an airfoil with sawtooth trailing-edge serrations is obtained. The far-field sound is then evaluated using the surface pressure integral based on the theories of Kirchhoff and Curle. The power spectral density (PSD) of the far-field sound is then related to the wavenumber spectral density of the hypothetical surface pressure under the turbulent boundary layer that would exist when the trailing-edge is absent. Numerical evaluation of the new model has shown better agreement than that obtained using Howe's model. Based on the new model, the sound reduction achieved by a trailing-edge with sharp sawtooth serrations is around 5-10 dB for a wide frequency range. This result better agrees with experiments, in which the average sound reduction is reported to be 5-7 dB. The results obtained using the new analytical model also agree well with FEM computations, suggesting that the model developed in this paper can capture the essential physics and give correct predictions for the sound generated by serrated trailing-edges. In the end, the physical mechanism of noise reduction is found to be the destructive interference effect of the scattered pressure field.

Nomenclature

$\mathbf{A}$	Coefficient matrix for $\mathbf{P}$ defined in Eq. 17
A_{ml}	Elements of matrix $\mathbf{A}$
a_n	Fourier coefficient of mode n
$\mathbf{B}$	Coefficient matrix for $\partial \mathbf{P}/\partial x$ defined in Eq. 17
B_{ml}	Elements of matrix $\mathbf{B}$
$\mathbf{C}^{(i)}$	Coupled part of solution in $\mathbf{P}$
c	Averaged chord length
c_0	Speed of sound
$C_{n'}^{(i)}$	Elements of vector $\mathbf{C}^{(i)}$
C_m	Dimensionless constant in Chase's model
$\mathcal{D}$	Linear differential operator
d	Span length
E	Complex error function
H	Serration profile function

[*]PhD Student, Department of Engineering, University of Cambridge, UK

[†]Lecturer, Royal Academy of Engineering Research Fellow, Department of Mechanical Engineering, University of Bristol, UK

[‡]Brunel Fellow, Royal Commission for the Exhibition of 1851, ISVR, University of Southampton, UK

h Half of root-to-tip length of serrations
i Imaginary symbol $\sqrt{-1}$
k Acoustic wavenumber ω/c_0
k_{2n} Characteristic wavenumber of mode n, $k_{2n} = k_2 + 2n\pi/\lambda$
k_1 Hydrodynamic wavenumber in chordwise direction
k_2 Hydrodynamic wavenumber in spanwise direction
$K_{n'}$ Transformed acoustic wavenumber of mode n'
$\mathcal{L}$ Gust-response function
$l_{y'}$ Correlation length in the y' direction
M_0 Mach number of uniform flow
$\mathbf{N}$ Non-coupled part of solution in $\mathbf{P}$
N $(2N+1)$ denoting the number of periods of serrations
N_0 An appropriate integer
$N_{n'}$ Elements of vector $\mathbf{N}$
$\bar{P}_{n'}$ Transformed scattered modal pressure
ΔP Pressure jump across the flat plate
$\mathbf{P}$ Vector expression of scattered pressure of different modes
P Time Fourier transformation of scattered pressure
p Scattered pressure field
P_{int} Hypothetical surface pressure beneath the turbulent boundary layer
$P_{n'}^{(i)}$ Elements of vector $\mathbf{P}^{(i)}$
p_i Incident wall pressure gust
p_f Far field sound pressure
$\hat{\mathbf{P}}^{(0)}$ Generalized pressure in vector form
$\mathbf{P}^{(i)}$ The i-th iterated solutions of PDEs
P_{ia} Magnitude of incident wall pressure gust
P_n Scattered pressure of mode n
Q_{nm} Function defined for expressing wall pressure gust response
R Function denoting phase relation in Eq. 42
S_0 $S_0 = \sqrt{x_1^2 + \beta^2(x_2^2 + x_3^2)}$
S_{nm} Function defined for expressing wall pressure gust response
S_{pp} PSD of far-field sound
S_{qq} Cross spectrum of surface pressure
T   Matrix transpose
T $2T$ as the time length used for Fourier transform defined in Eq. 54
t Time
U Uniform flow velocity
U_c Turbulence convection velocity
v_* Friction velocity in Chase's model
x Chordwise axis in stretched coordinate system
x' Chordwise axis in airfoil-fixed frame
x_1 The projection of observer point on x'
x_2 The projection of observer point on y'
x_3 The projection of observer point on z'
y Spanwise axis in stretched coordinate system
y' Spanwise axis in airfoil-fixed frame
z Axis perpendicular to airfoil in stretched coordinate system
z' Axis perpendicular to airfoil in airfoil-fixed frame

Subscripts

j The j-th edge of a single piece of sawtooth serrations

Conventions

FEM   Finite Element Method
PDE   Partial Differential Equation
PML   Perfectly Matched Layer

American Institute of Aeronautics and Astronautics

PSD	Power Spectral Density
SWL	Sound poWer Level

Symbols

$\boldsymbol{\alpha}$	Coefficient matrix in the first-order results
β	$\beta = \sqrt{1 - M_0^2}$
β_{ln}	Coefficient in the high-order results
χ	Dimensionless constant in Chase's model
δ	Boundary layer thickness
δ	Conventional generalized function in Eq. 56 and Sec. B
δ	Generalized function defined in Eq. 34
δ_{ml}	The Kronecker delta
ϵ_j	The chordwise coordinate of the starting point of the j-th edge
ϵ_{j+1}	The chordwise coordinate of the ending point of the j-th edge
η_{Am}	Wavenumber in S_{nm}
η_{Bmj}	Wavenumber in S_{nm}
Γ	Properly bounded complex function
γ_{ln}	Coefficient in the high-order results
κ_{nj}	Wavenumber in Q_{nm}
λ	Wavelength of serrations
λ_j	The spanwise coordinate of the starting point of the j-th edge
λ_{j+1}	The spanwise coordinate of the ending point of the j-th edge
μ_A	Wavenumber in Q_{nm}
μ_{Bnj}	Wavenumber in Q_{nm}
$\mu_{n'}$	Transformed mixed wavenumber of mode n'
ω	Angular frequency $\omega = 2\pi f$
ϕ	Angle defined in Fig. 3
Π	Wavenumber spectral density
Ψ	Normalized power spectrum of far-field sound
Ψ_f	Normalized power spectrum in Howe's model in Eq. 71
ρ_0	Fluid density
σ_j	Slope of the j-th edge
σ	Absolute value of the slope of a sawtooth edge
τ	Variable in function $\delta(x - \tau)$
θ	Fly-over angle defined in Fig. 3
$\Theta_{n'}$	Fundamental order of the gust-response function
$\Theta_{n'}^{(i)}$	i-th order of the gust-response function
ξ	Integral variable

Superscripts

$'$	First derivative of function
$''$	Second derivative of function

I.   Introduction

The past few decades has seen a rapid growth of air traffic, while the public sensitivity to aircraft noise has also been continuously increasing. This has led to more stringent regulations for aircraft noise.[1] With regard to the impact of aircrafts on community noise, the take-off and landing process are of main concern. Among the different mechanisms present during the landing process, airframe noise is believed to be the dominant component. It is now widely accepted that the broadband noise, induced by the interaction of boundary layer with the airfoil trailing-edge, known as the turbulent boundary

Figure 1: Schematic illustration of the trailing-edge noise

layer trailing-edge noise, plays a significant role in the overall airframe noise. Nowadays, wind energy is being used globally[2] as a green alternative to the traditional energy forms. And it is found that the turbulent boundary layer trailing-edge noise also dominates the noise produced by wind turbines. Extensive research has thus been conducted in recent years, in the hope of understanding the noise generation mechanism and developing new techniques to reduce it. Unless explicitly stated, from now on the turbulent boundary layer trailing-edge noise will be referred to as the trailing-edge noise.

When a turbulent boundary layer convects past the trailing-edge, the unsteady pressure with a wavenumber in the hydrodynamic range is scattered into sound with the wavenumbers in the acoustic range, leading to noise radiated from trailing-edge,[3] as shown in Fig. 1. Both experiments and theories reveal that the radiated sound power varies with the characteristic flow velocity to the power of five, which is thus more efficient than that when the airfoil is absent at low Mach numbers.[4]
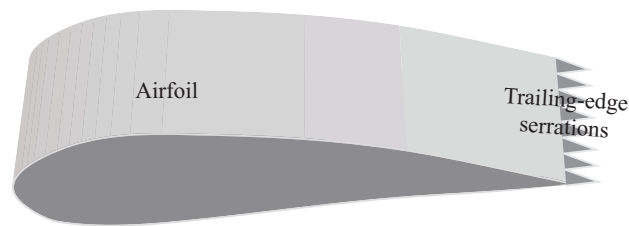

Figure 2: Schematic figure of trailing-edge serrations

As the trailing-edge noise dominates the sound generation at low Mach numbers, different noise control techniques have been investigated. The most widely studied method for trailing-edge noise reduction is using serrated trailing-edges.[5,6] Figure 2 shows an airfoil with the serrations of a sawtooth profile appended at the trailing-edge. The use of serrations in airfoil configurations was reviewed in both Howe and Gruber's papers.[7,6] The concept of sawtooth serration was proposed by Ver,[8] and was reported to reduce the jet exhaust noise by about 5 dB. Later experiment found that the serrations applied to leading-edges can be effective to reduce the correlation length of turbulence near the trailing-edge, but can also result in adverse effects on the airfoil lift.[9,10] Inspired by leading-edge serrations, Howe proposed a theoretical model to predict the sound generated by the serrated trailing-edge of both the sinusoidal and sawtooth profiles.[7,11] It was shown that sawtooth serrations are more effective in reducing the trailing-edge noise than the sinusoidal ones, and the use of sharp sawtooth serrations can lead to significant trailing-edge noise reduction. Quite recently, Azarpeyvand et al.[12] investigated analytically the trailing-edge noise reduction using novel serrations, namely, sawtooth, sinusoidal, slitted, slitted-sawtooth and sawtooth-sinusoidal. It has been found that the noise reduction is a sensitive function of the complexity of the serration geometry and significant noise reduction can be achieved by applying complex periodic serrations to the trailing-edge. It has also been shown that the slitted-sawtooth serration is the most effective design among the aforementioned serrations geometries.

An experimental investigation on trailing-edge serrations was performed by Dassen et al.[13] in 1996. Both airfoils and flat-plates of different shapes were tested in a wind tunnel. A maximum of 10 dB reduction for the flat plate and 8 dB reduction for the airfoil were reported, both of which occurred mainly at low frequencies. Later, Parchen et al.[5] conducted an experimental investigation of the aeroacoustic effects of trailing-edge serrations on wind turbine blades at both full and wind-tunnel scales. An average sound reduction slightly below that reported by Dassen et al. was observed. Most recently, Oerlemans et al.[14] examined and compared the noise generated by serrated airfoils and aeroacoustically optimized ones, but only 2-3 dB noise reduction was achieved. Both Parchen et al. and Oerlemans et al. found noise increase at high frequencies and attributed this to the misalignment of serrations.

Gruber[6] recently conducted extensive experimental tests on the aeroacoustic performance of airfoils using different sawtooth serrations. The acoustic measurements were performed to give the Sound Power Level (SWL) integrated in the mid-span plane. An average of 3-5 dB reduction was achieved using sharp sawtooth serrations, and a noise increase of up to 5 dB at higher frequencies was also reported. It was explained that the significant reduction of phase speed near the sawtooth edges, together with a slight reduction of the coherence of pressure measured along the edge, is responsible for the sound reduction observed in experiments. All the experimental studies, however, indicate that Howe's model significantly overpredicts the sound reduction capability of trailing-edge serrations. This might be caused by the assumptions and approximations in Howe's derivation, which will be discussed in detail in this paper.

Although different serrations have been used in many applications such as wind turbines and jet nozzles,[14,15,16] the physical mechanism of the noise reduction is yet to be further clarified. Howe's model gave a first insight into the physics involved, but the large deviation from experimental results suggests a new and more accurate theory is needed.

The main objectives of this paper are to develop a new theory to predict sound generated by a serrated trailing-edge more accurately, and to improve our understanding of the sound reduction mechanism due to the presence of trailing-edge serrations.

The paper is structured as follows: Sec. II introduces the idea of the newly extended model, and provides a detailed derivation. In Sec. III, the new analytical model is validated by comparing with FEM computations and the dependence of the noise reduction on the geometrical parameters of serrations is also discussed. Sec. IV presents the main results obtained using the new model. A direct comparison between this model and Howe's model is made in Sec. V while the following section briefly discusses the physical mechanism of sound reduction using trailing-edge serrations. In the last section of this paper, a short conclusion is given.

II.   Analytical formulation

In this section, we present a detailed derivation for the noise prediction of serrated trailing-edges. The analytical model developed as part of this research work for serrated airfoils is based on Amiet's model and Schwarzschild technique for solving the wave equation with appropriate boundary conditions.

A.   The mathematical model

Similar to Amiet's model,[17,18] the Schwarzschild technique is used in this model to solve a special type of boundary-value problem. Thus it is convenient to describe it in the first place. The Schwarzschild technique states[19,17,18] that, if the function $f(x, y)$ satisfies

$$
\begin{cases}
\dfrac{\partial^2 f}{\partial x^2} + \dfrac{\partial^2 f}{\partial y^2} + \mu^2 f = 0 \\[2mm]
\dfrac{\partial f}{\partial y}(x, 0) = 0, & x < 0 \\[2mm]
f(x, 0) = f_0(x), & x \geq 0,
\end{cases}
\tag{1}
$$

then, for $x < 0$,

$$
f(x, 0) = \frac{1}{\pi} \int_0^\infty \sqrt{\frac{-x}{\xi}} \, \frac{e^{i\mu(\xi - x)}}{\xi - x} \, f_0(\xi) \, \mathrm{d}\xi.
\tag{2}
$$

Now consider an airfoil with trailing-edge serrations as an infinitesimally thin plate as shown in Fig. 3 with an averaged chord length c and spanwise length d. Let x' and y' denote the streamwise and spanwise coordinates, respectively. The direction perpendicular to the airfoil plane is parallel to the z' axis. The observer point, as shown in Fig. 3, is located at (x_1, x_2, x_3).

The profile function $H(y')$ is used to describe the serrated edges. And the origin of the coordinates is chosen in such a way that $H(y')$ is an oscillatory function of zero mean and that $H(y') = 0$ in the absence of serrations. Figure 3 shows a sawtooth serration with the root-to-tip length of $2h$ and the periodic wavelength of λ. In this case let σ, defined as $4h/\lambda$ to quantify the sharpness of the sawtooth serrations.

When the acoustic wavelength is equal to or smaller than the chord length c, the flat plate shown in Fig. 3 can be treated as an infinitely long plate

Figure 3: Sketch of the airfoil with a serrated trailing-edge and the coordinate system

without a leading-edge.[17,18,20] Also, the airfoil is considered infinite in the spanwise direction when it has a relatively large aspect ratio (typically larger than 3).[18,21] The turbulence inside the boundary layer is assumed to be frozen: it remains statistically the same before and after passing over the trailing-edge.

Now consider the hypothetical surface pressure beneath the turbulent boundary layer that would exist when the trailing-edge is absent. After implementing a spatial and time Fourier transformation, the surface
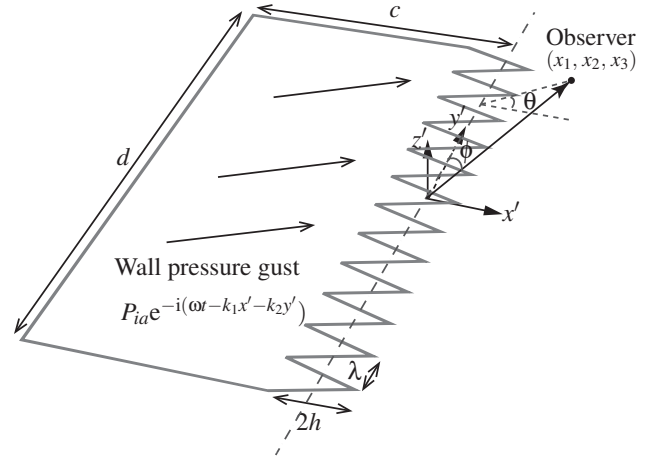
American Institute of Aeronautics and Astronautics

pressure can be expressed as an integral of different wall pressure gust components. The specific component of frequency ω as illustrated in Fig. 3 takes the form of

$$p_i = P_{ia}e^{-i(\omega t - k_1 x' - k_2 y')}, \tag{3}$$

where, P_{ia} is the magnitude of the incident wall pressure gust and k_1 and k_2 denote the wavenumbers in the chordwise and spanwise directions, respectively.

According to Curle,[22] a solid boundary will induce an extra distribution of dipole sources while only quadrupole sources exist when no boundary is present in an unbounded fluid. Amiet[17] explained that the presence of the half-rigid surface leads to a scattered pressure distribution, which exactly cancels the dipole distribution that otherwise exists. The total pressure may then be decomposed into an incident part p_i and a scattered part p, such that the total pressure can be expressed as the sum of p_i and p. The incident pressure, p_i, is given in Eq. 3, and the boundary conditions at $z' = 0$ now read

$$\begin{cases} \dfrac{\partial p}{\partial z'} = 0, & x' < H(y') \\ p = -P_{ia}e^{-i(\omega t - k_1 x' - k_2 y')}, & x' \geq H(y'). \end{cases} \tag{4}$$

In the airfoil-fixed frame $\{x', y', z'\}$, the wave equation governing the scattered pressure field p remains the same as in the straight-edge cases, namely

$$\nabla^2 p - \frac{1}{c_0^2}\left(\frac{\partial}{\partial t} + U\frac{\partial}{\partial x'}\right)^2 p = 0, \tag{5}$$

where c_0 denotes the speed of sound. With the assumption of harmonic perturbation $p = P(x', y', z')e^{-i\omega t}$, the above equation reduces to

$$\beta^2 \frac{\partial^2 P}{\partial x'^2} + \frac{\partial^2 P}{\partial z'^2} + \frac{\partial^2 P}{\partial y'^2} + 2ikM_0\frac{\partial P}{\partial x'} + k^2 P = 0, \tag{6}$$

where, $k = \omega/c_0$, $\beta^2 = 1 - M_0^2$ and $M_0 = U/c_0$.

In order to make the boundary conditions in Eq. 4 independent of y', the coordinate transformation[23] $x = x' - H(y'), y = y', z = z'$ is used and leads to the following differential equation:

$$\left(\beta^2 + H'^2(y)\right)\frac{\partial^2 P}{\partial x^2} + \frac{\partial^2 P}{\partial y^2} + \frac{\partial^2 P}{\partial z^2} - 2H'(y)\frac{\partial^2 P}{\partial x \partial y} + (2iM_0 k - H''(y))\frac{\partial P}{\partial x} + k^2 P = 0, \tag{7}$$

where, $H'(y)$ and $H''(y)$ denote the first and second derivatives of $H(y)$. The boundary conditions now read

$$\begin{cases} P(x, y, 0) = -P_{ia}e^{i(k_1 x + k_2 y)}e^{ik_1 H(y)}, & x \geq 0 \\ \partial P(x, y, 0)/\partial z = 0, & x < 0. \end{cases} \tag{8}$$

Unlike the governing equation for a straight trailing-edge,[20] the coefficients in Eq. 7 depend on y, and therefore using the "separation of variables" technique to solve this equation becomes rather difficult, if not impossible. Therefore, we shall employ the Fourier expansion technique, as explained in the following section.

B. Fourier expansion

Considering both the infinite-span assumption and the serration periodicity, one can thus expand the scattered pressure using Fourier series in terms of the new coordinates (x, y, z), as

$$P(x, y, z) = \sum_{-\infty}^{\infty} P_n(x, z)e^{ik_{2n}y}, \tag{9}$$

where, $k_{2n} = k_2 + 2n\pi/\lambda$.

Substituting the above expression into the transformed wave equation, shown in Eq. 7, yields

$$\left\{ \left(\beta^2 + H'^2(y) \right) \frac{\partial^2}{\partial x^2} + \frac{\partial^2}{\partial y^2} + \frac{\partial^2}{\partial z^2} - 2H'(y) \frac{\partial^2}{\partial x \partial y} + (2iM_0 k - H''(y)) \frac{\partial}{\partial x} + k^2 \right\}$$

$$\sum_{-\infty}^{\infty} P_n(x,z) e^{ik_{2n}y} = 0. \tag{10}$$

Multiplying Eq. 10 by $e^{-ik_{2n'}y}$, then integrating it over y from $-\lambda/2$ to $\lambda/2$, it can be readily shown that

$$\left\{ \beta^2 \frac{\partial^2}{\partial x^2} + \frac{\partial^2}{\partial z^2} + 2ikM_0 \frac{\partial}{\partial x} + (k^2 - k_{2n'}^2) \right\} P_{n'}$$

$$+ \frac{1}{\lambda} \int_{-\lambda/2}^{\lambda/2} \sum_{n=-\infty}^{\infty} \left\{ H'^2 \frac{\partial^2}{\partial x^2} - (H'' + 2ik_{2n}H') \frac{\partial}{\partial x} \right\} P_n e^{i2(n-n')\pi/\lambda y} \, \mathrm{d}y = 0. \tag{11}$$

The only way to obtain an equation which only involves one mode, say n', is when both $H'(y)$ and $H''(y)$ are constants within the entire wavelength, so that the summation over different modes in Eq. 11 can be dropped. For serrations of a sawtooth profile, $H'(y)$ is not continuous and hence $H''(y)$ is singular at the joint-points. We use the generalized function $\delta(y)$ to describe the singularities. As $\int_{-\infty}^{\infty} \delta(x)f(x)\,\mathrm{d}x = f(0)$, the summation in Eq. 11 can not be dropped, hence different modes are coupled together.

In this paper, we only focus on the sawtooth serration, which has been shown to be more effective in reducing the trailing-edge noise than the sinusoidal one.[11] However the method can also be used for other serrations. Consider the single piece of sawtooth centered around the coordinate origin, and let (λ_0, ϵ_0), (λ_1, ϵ_1) and (λ_2, ϵ_2) denote the three joint-points connected with this sawtooth, as shown in Fig. 4. The serration profile function $H(y)$ can therefore be defined as

Figure 4: The schematic of serration profile

$$H(y) = \begin{cases} \sigma_0(y - \lambda_0 - m\lambda) + \epsilon_0, & \lambda_0 + m\lambda < y \le \lambda_1 + m\lambda \\ \sigma_1(y - \lambda_1 - m\lambda) + \epsilon_1, & \lambda_1 + m\lambda < y \le \lambda_2 + m\lambda \end{cases} \tag{12}$$

where, $\sigma_j = (\epsilon_{j+1} - \epsilon_j)/(\lambda_{j+1} - \lambda_j)$, $j = 0, 1$ and $m = 0, \pm 1, \pm 2, \pm 3 \cdots$. For a sawtooth profile, as mentioned above, $H'(y)$ is not continuous and $H''(y)$ is thus singular at the joint-points. We use the conventional generalized function $\delta(x)$ to describe the singularities at these points, i.e.

$$H'(y) = \begin{cases} \sigma_0, & \lambda_0 + m\lambda < y \le \lambda_1 + m\lambda \\ \sigma_1, & \lambda_1 + m\lambda < y \le \lambda_2 + m\lambda \end{cases}$$

$$H''(y) = \sum_{m=-\infty}^{\infty} (-1)^{m+1} 2\sigma\delta(x - m\lambda/2). \tag{13}$$

Substituting the serration profile function and its derivatives, Eqs. 12 and 13, into the wave equation, Eq. 11, and making use of the fact that $\int_{-\infty}^{\infty} f(x)\delta(x - \tau)\,\mathrm{d}x = f(\tau)$, we obtain

$$\left\{ (\beta^2 + \sigma^2) \frac{\partial^2}{\partial x^2} + \frac{\partial^2}{\partial z^2} + 2ikM_0 \frac{\partial}{\partial x} + (k^2 - k_{2n'}^2) \right\} P_{n'}$$

$$= -\frac{4\sigma}{\lambda} \sum_{n-n'=odd} \left(1 - \frac{k_2\lambda + 2n\pi}{(n-n')\pi} \right) \frac{\partial P_n}{\partial x}. \tag{14}$$
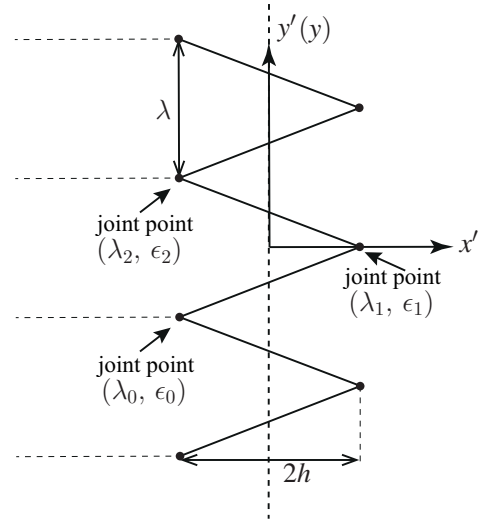
American Institute of Aeronautics and Astronautics

We can write the set of differential equations obtained above in a more compact matrix form. Let a linear operator

$$\mathcal{D} = \left\{ (\beta^2 + \sigma^2)\frac{\partial^2}{\partial x^2} + \frac{\partial^2}{\partial z^2} + 2ikM_0\frac{\partial}{\partial x} \right\}, \tag{15}$$

and a vector of functions

$$\mathbf{P} = (\cdots P_{-n'}(x,z),\ P_{-n'+1}(x,z),\ \cdots P_{n'-1}(x,z),\ P_{n'}(x,z),\ \cdots)^{\mathrm{T}}, \tag{16}$$

then the coupled equations can be written as

$$\mathcal{D}\mathbf{P} = \mathbf{A}\mathbf{P} + \mathbf{B}\frac{\partial \mathbf{P}}{\partial x}, \tag{17}$$

where the symbol T in Eq. 16 denotes the transpose of a matrix. Matrices $\mathbf{A}$ and $\mathbf{B}$ denote the coefficient matrices of $\mathbf{P}$ and $\partial\mathbf{P}/\partial x$, respectively, and A_{ml} and B_{ml} representing the entry corresponding to mode m in row and l in column of matrix $\mathbf{A}$ and $\mathbf{B}$ are given by

$$A_{ml} = (k_{2m}^2 - k^2)\delta_{ml}, \quad B_{ml} = \begin{cases} \dfrac{4\sigma}{\lambda}\dfrac{m+l+k_2\lambda/\pi}{l-m}, & m-l = odd \\ 0, & m-l = even, \end{cases} \tag{18}$$

where δ_{ml} represents the Kronecker delta.

Upon the substitution of the profile geometry, Eq. 12, into the boundary conditions, Eq. 8, and performing the same Fourier expansions, we obtain

$$\begin{cases} P_n(x,0) = -P_{ia}a_n e^{ik_1 x}, & x > 0 \\ \dfrac{\partial P_n}{\partial z}(x,0) = 0, & x \le 0, \end{cases} \tag{19}$$

where, a_n is defined as

$$a_n = \frac{1}{\lambda}\int_{-\lambda/2}^{\lambda/2} e^{ik_1 H(y)} e^{-i2n\pi/\lambda y}\,\mathrm{d}y. \tag{20}$$

In Eq. 17, as $\mathbf{B}$ is not a diagonal matrix, the term $\mathbf{B}(\partial\mathbf{P}/\partial x)$ contains coupling terms, in the sense that P_n for example, appears in the governing equation of P_m. This means every mode is interacting with the other modes and can not be solved individually. From the expression of $\mathbf{B}$ in Eq. 18, it can be seen that the strength of coupling is proportional to σ/λ. This indicates that shaper serrations have stronger coupling between different modes. Note that $\mathbf{A}$ is already a diagonal matrix. So, if $\mathbf{B} \approx 0$, i.e. the coupling effect vanishes completely, and we can solve each mode individually.

At very low frequencies, it is expected that the contribution of higher modes is negligible compared with the 0-th mode. Thus, for the equation governing the 0-th mode, the coupling with higher modes becomes weak. One can thus solve the 0-th mode individually, and calculate the surface pressure with only the contribution of the 0-th mode. But this only works for very low frequencies or for very wide serrations. The coupling effect becomes more pronounced at high frequencies. To solve these coupled equations at relatively high frequencies, we will use an iterative solving procedure, as explained in the following section.

C.   Acoustic formulation

Following the same procedure used by Amiet,[17,18] in this section the scattered surface pressure is solved first and the far-field sound is then evaluated based on the theories of Kirchhoff and Curle.[22]

1.   Scattered surface pressure

To obtain the scattered surface pressure, Eq. 17 together with the boundary conditions in Eq. 19 need to be solved. Recall a set of linear algebraic equations, it is known that its solution can be sought via the so-called iteration process.[24] One can draw an analogy between these PDEs and those linear algebraic equations, the solutions to a set of PDEs may thus be found in an iterative manner similarly.

American Institute of Aeronautics and Astronautics

Substituting an assumed initial value $\mathbf{P}^{(0)}$ into the coupling term in Eq. 17, one can obtain

$$\mathcal{D}\mathbf{P} = \mathbf{A}\mathbf{P} + \mathbf{B}\frac{\partial \mathbf{P}^{(0)}}{\partial x}. \tag{21}$$

Solving Eq. 21 gives a new set of solutions $\mathbf{P}^{(1)}$. Replacing $\mathbf{P}^{(0)}$ in Eq. 21 with $\mathbf{P}^{(1)}$, we obtain a new wave equation,

$$\mathcal{D}\mathbf{P} = \mathbf{A}\mathbf{P} + \mathbf{B}\frac{\partial \mathbf{P}^{(1)}}{\partial x}. \tag{22}$$

Solving Eq. 22 gives a new set of solutions $\mathbf{P}^{(2)}$. Continuing this process, we obtain a solution sequence, $\mathbf{P}^{(0)}$, $\mathbf{P}^{(1)}$, $\mathbf{P}^{(2)}$, $\mathbf{P}^{(3)} \cdots$. If the sequence appears to be convergent, we manage to obtain the solution to Eq. 17.

The initial value $\mathbf{P}^{(0)}$ used to start the first iteration can be found by ignoring all the coupling terms, i.e. with $\mathbf{B} = 0$, and by solving each equation individually using the standard Schwarzschild technique. Therefore, the solution to each equation in the uncoupled matrix equation

$$\mathcal{D}\mathbf{P} = \mathbf{A}\mathbf{P} \tag{23}$$

can be found as follows.

After use is made of the transformation of $P_{n'} = \bar{P}_{n'} e^{-ikM_0/(\beta^2 + \sigma^2)x}$, individual equations in Eq. 23 reduces to,

$$\{(\beta^2 + \sigma^2)\frac{\partial^2}{\partial x^2} + \frac{\partial^2}{\partial z^2} + K_{n'}^2(\beta^2 + \sigma^2)\}\bar{P}_{n'} = 0, \tag{24}$$

where,

$$K_{n'} = \sqrt{k^2(1 + \sigma^2) - k_{2n'}^2(\beta^2 + \sigma^2)}/(\beta^2 + \sigma^2). \tag{25}$$

Making use of $X = x, Z = \sqrt{\beta^2 + \sigma^2}z$, one can verify that Eq. 24 reduces to a standard Schwarzschild problem, and the solution can be found using the Schwarzschild integral described in Eq. 2 as

$$P_{n'}^{(0)} = P_{ia}e^{ik_1 x}a_{n'}\big((1 - i)E(-\mu_{n'}x) - 1\big), \tag{26}$$

where $P_{n'}^{(0)}$ is the element of vector $\mathbf{P}^{(0)}$ corresponding to the n'-th mode, and

$$\mu_{n'} = K_{n'} + k_1 + \frac{kM_0}{\beta^2 + \sigma^2},$$
$$E(x) = \int_0^x \frac{e^{it}}{\sqrt{2\pi t}}\,\mathrm{d}t. \tag{27}$$

The initial solutions obtained by ignoring all the coupling terms denote the non-coupled part of the exact solution of each mode, which implies that an n-th mode excitation $(x > 0)$ produces only an n-th mode response $(x < 0)$. The iteration procedure will add a coupled part to the solution of each mode. The coupled part implies that an n-th mode input $(x > 0)$ will also produce some m-th mode response $(x < 0)$, where $n \neq m$.

As discussed above, by substituting $\mathbf{P}^{(0)}$ into the coupling terms on the right hand side of Eq. 17, one obtains

$$\mathcal{D}\mathbf{P} = \mathbf{A}\mathbf{P} + \mathbf{B}\frac{\partial \mathbf{P}^{(0)}}{\partial x}. \tag{28}$$

However, these equations can not be solved using the standard Schwarzschild technique, since they are inhomogeneous equations. But if one can manipulate these equations so that they change to homogeneous ones, Schwarzschild's method can again be used. Note that $\mathbf{P}^{(0)}$ satisfies Eq. 23, hence, for $x \neq 0$, where $\mathbf{P}^{(0)}$ is first-order continuously differentiable, the following equation holds:

$$\mathcal{D}\frac{\partial \mathbf{P}^{(0)}}{\partial x} = \mathbf{A}\frac{\partial \mathbf{P}^{(0)}}{\partial x}. \tag{29}$$

Making use of Eq. 29, Eq. 28 can be equivalently written as

$$\mathcal{D}(\mathbf{P} + \boldsymbol{\alpha}\frac{\partial \mathbf{P}^{(0)}}{\partial x}) = \mathbf{A}(\mathbf{P} + \boldsymbol{\alpha}\frac{\partial \mathbf{P}^{(0)}}{\partial x}), \tag{30}$$

American Institute of Aeronautics and Astronautics

where, $\boldsymbol{\alpha}$ is a coefficient matrix whose entry is

$$\alpha_{ml} = \frac{B_{ml}}{k_{2m}^2 - k_{2l}^2} = \begin{cases} \dfrac{-4h}{\pi^2(m-l)^2}, & m - l = odd \\ 0, & m - l = even. \end{cases} \tag{31}$$

It is worth pointing out that Eq. 30 only holds when $x \neq 0$, not for $x \in \mathbf{R}$. In order to apply the Schwarzschild's technique, it must be valid over the whole domain. However, since the singularity of $\partial \mathbf{P}^{(0)}/\partial x$ only exists at $x = 0$, similar to the differentiation of $H(y)$, we may again make use of the generalize function to account for this singularity. Let $\partial \hat{\mathbf{P}}^{(0)}/\partial x$ denote the generalized differentiation, which allows the presence of generalized functions at singular point $x = 0$ but equals to $\partial \mathbf{P}^{(0)}/\partial x$ elsewhere, then equation

$$\mathcal{D}\frac{\partial \hat{\mathbf{P}}^{(0)}}{\partial x} = \mathbf{A}\frac{\partial \hat{\mathbf{P}}^{(0)}}{\partial x} \tag{32}$$

needs to hold for any $x \in \mathbf{R}$. The Schwarzschild technique suggests that if Eq. 32 does hold, then routine application of the steps described from Eq. 24 to Eq. 26 shall recover the value of $\partial \mathbf{P}^{(0)}/\partial x$ for $x < 0$. Thus, one can verify that the intended $\partial \hat{\mathbf{P}}^{(0)}/\partial x$ can indeed be found as

$$\frac{\partial \hat{P}_{n'}^{(0)}}{\partial x}(x,0) = \frac{\partial P_{n'}^{(0)}}{\partial x}(x,0) + P_{ia}a_{n'}(1-i)(-\sqrt{\mu_{n'}})\sqrt{2\pi x}\delta(x), \tag{33}$$

where, $\partial \hat{P}_{n'}^{(0)}/\partial x$ denotes the element of $\partial \hat{\mathbf{P}}^{(0)}/\partial x$ corresponding to the n'-th mode and

$$\int_0^\infty \delta(x)\,\mathrm{d}x = \frac{1}{2}. \tag{34}$$

Now the first iterated solution can be obtained by solve equation

$$\mathcal{D}(\mathbf{P} + \frac{\partial \hat{\mathbf{P}}^{(0)}}{\partial x}) = \mathbf{A}(\mathbf{P} + \frac{\partial \hat{\mathbf{P}}^{(0)}}{\partial x}), \tag{35}$$

via steps described from Eq. 24 to Eq. 26.

Solving Eq. 35 gives the values of $\mathbf{P}^{(1)}$. Continuing this iteration process gives $\mathbf{P}^{(2)}$, $\mathbf{P}^{(3)}$, ..., and the exact solutions $\mathbf{P}$ can be expressed as

$$\mathbf{P}(x,0) = \mathbf{N}(x) + \mathbf{C}^{(1)}(x) + \mathbf{C}^{(2)}(x) + \mathbf{C}^{(3)}(x) + \cdots, \tag{36}$$

where the non-coupled part is denoted by $\mathbf{N}$, while the coupled parts are denoted by $\mathbf{C}^{(i)}$ ($i = 1, 2, 3 \cdots$). Here only the entries of $\mathbf{N}$ and $\mathbf{C}^{(1)}$ corresponding to mode n' are presented, which are

$$N_{n'}(x) = P_{ia}e^{ik_1 x}a_{n'}\left((1-i)E(-\mu_{n'}x) - 1\right) \tag{37}$$

and

$$C_{n'}^{(1)}(x) = P_{ia}e^{ik_1 x}(1-i)\sum_{m=-\infty}^{\infty}\alpha_{n'm}a_m\left(ik_1\Big(E(-\mu_{n'}x) - E(-\mu_m x)\Big)\right.$$
$$\left. -\sqrt{\frac{\mu_m}{-2\pi x}}\Big(e^{-i\mu_{n'}x} - e^{-i\mu_m x}\Big)\right) \tag{38}$$

respectively.

The results of the second iteration is rather complex and can be found in Appendix A. It is worth nothing that function $\mathbf{C}^{(i)}$ becomes more and more complex as i increases. However, if $\mathbf{C}^{(i)}$ vanishes sufficiently quickly, higher order can be cut off without causing significant errors. This appears to be the case at least at sufficiently low frequencies considered in this paper.

Substituting Eqs. 37 and 38 into Eq. 36, a first-order approximation of the exact solutions is obtained. The scattered surface pressure is finally obtained by summing the modal pressure over all different modes and transforming back to the physical coordinate system, namely

$$P(x', y', 0) = \sum_{n'=-\infty}^{\infty} P_{n'}(x' - H(y'), 0)e^{ik_{2n'}y'}. \tag{39}$$

American Institute of Aeronautics and Astronautics

Here, $P_{n'}$ is the solution obtained from the iteration procedure mentioned above, namely

$$P(x', y', 0) = \sum_{n'=-\infty}^{\infty} [N_{n'} + C_{n'}^{(1)} + C_{n'}^{(2)} + \cdots](x' - H(y'), 0)e^{ik_{2n'}y'}, \tag{40}$$

where the $N_{n'}$ and $C_{n'}^{(1)}$ functions are defined in Eq. 37 and Eq. 38 respectively, $C_{n'}^{(2)}$ can be found in the appendix and the terms in the second parenthesis are the arguments for the $N_{n'}$ and $C_{n'}^{(i)}$ ($i = 1, 2, 3, \cdots$) functions.

As shown in Eq. 40, the scattered pressure field can now be expressed in terms of an infinite series. In a limiting case when $h = 0$, all the $C_{n'}^{(i)}$ ($i = 1, 2, 3 \cdots$) terms on the right hand side of Eq. 40 vanish, and Amiet's result is recovered. It is worth noting that the term $C_{n'}^{(i)} \propto h^i$, where $i = 1, 2, 3, \cdots$, thus Eq. 40 may be understood as a perturbation solution with respect to h. It can be shown that at sufficiently low frequencies, i.e. $k_1 h < \pi^2/4$, the infinite series converges. At higher frequencies, the series still appears to be convergent, but it can be expected that for a proper approximation, a higher truncation number and higher-order iterations are required. In what follows, we assume that at the frequencies of interest the infinite series shown in Eq. 40 is convergent.

2. Far-field sound pressure

Having obtained the scattered surface pressure, the far field sound induced by the scattered surface pressure can be found using the surface pressure integral, as

$$p_f(\mathbf{x}, \omega) = \frac{-i\omega x_3}{4\pi c_0 S_0^2} \iint_s \Delta P(x', y')e^{-ikR} \, dx' \, dy', \tag{41}$$

where $S_0^2 = x_1^2 + \beta^2(x_2^2 + x_3^2)$, and R takes the following form:

$$R = \frac{M_0(x_1 - x') - S_0}{\beta^2} + \frac{x_1 x' + x_2 y' \beta^2}{\beta^2 S_0}, \tag{42}$$

where, as explained above, the pressure jump $\Delta P = P$, given by Eq. 40.

By substituting the solution obtained in Eq. 40 into Eq. 41, the far-field sound pressure can be found as

$$p_f(\mathbf{x}, \omega, k_2) = \left(\frac{-i\omega x_3 c}{4\pi c_0 S_0^2}\right) \lambda \frac{\sin\left((N + 1/2)\lambda(k_2 - kx_2/S_0)\right)}{\sin\left(\lambda/2(k_2 - kx_2/S_0)\right)} \mathcal{L}(\omega, k_2) P_{ia}. \tag{43}$$

Here, $2N + 1$ represents the number of sawtooth on the edge and the non-dimensional far-field sound gust-response function $\mathcal{L}$ is defined as

$$\mathcal{L}(\omega, k_2) = (1 - i)\frac{1}{\lambda c}\left(\sum_{n'=-\infty}^{\infty}\left(\Theta_{n'} + \Theta_{n'}^{(1)} + \Theta_{n'}^{(2)} + \cdots\right)\right)e^{-ik/\beta^2(M_0 x_1 - S_0)}e^{ik/\beta^2(M_0 - x_1/S_0)h}, \tag{44}$$

with (only the first two terms are given, see more results in the appendix)

$$\begin{aligned}
\Theta_{n'} &= a_{n'} Q_{n'n'}; \\
\Theta_{n'}^{(1)} &= \sum_{m=-\infty}^{\infty} \alpha_{n'm} ik_1 a_m (Q_{n'n'} - Q_{n'm}) - \alpha_{n'm}\sqrt{\mu_{n'}} a_m (S_{n'n'} - S_{n'm}).
\end{aligned} \tag{45}$$

The function Q_{nm} and S_{nm} in the above equations are given by

$$\begin{aligned}
Q_{nm} = \sum_{j=0}^{1} \frac{1}{\kappa_{nj}} \Big(&\frac{1}{\mu_A}\left(e^{i\kappa_{nj}\lambda_{j+1}}\Gamma(c + \epsilon_{j+1}; \mu_m, \mu_A) - e^{i\kappa_{nj}\lambda_j}\Gamma(c + \epsilon_j; \mu_m, \mu_A)\right) \\
&- \frac{1}{\mu_{Bnj}}e^{i\kappa_{nj}(\lambda_j - (c+\epsilon_j)/\sigma_j)}\left(\Gamma(c + \epsilon_{j+1}; \mu_m, \mu_{Bnj}) - \Gamma(c + \epsilon_j; \mu_m, \mu_{Bnj})\right)\Big),
\end{aligned} \tag{46}$$

$$S_{nm} = \sum_{j=0}^{1} \frac{1}{i\kappa_{nj}} \left(\frac{1}{\sqrt{\eta_{Am}}} \left(e^{i\kappa_{nj}\lambda_{j+1}} E(\eta_{Am}(c + \epsilon_{j+1})) - e^{i\kappa_{nj}\lambda_j} E(\eta_{Am}(c + \epsilon_j)) \right) \right.$$
$$\left. - \frac{1}{\sqrt{\eta_{Bmj}}} e^{i\kappa_{nj}(\lambda_j - (c + \epsilon_j)/\sigma_j)} \left(E(\eta_{Bmj}(c + \epsilon_{j+1})) - E(\eta_{Bmj}(c + \epsilon_j)) \right) \right),$$

where

$$\Gamma(x; \mu, \nu) = e^{-i\nu x} E(\mu x) - \sqrt{\frac{\mu}{\mu - \nu}} E((\mu - \nu)x) + \frac{1}{1 - i}(1 - e^{-i\nu x}), \tag{47}$$

$$\begin{aligned}
\eta_{Am} &= K_m + kM_0/(\beta^2 + \sigma^2) - k/\beta^2(M_0 - x_1/S_0), \\
\eta_{Bmj} &= K_m + kM_0/(\beta^2 + \sigma^2) + (k_{2n} - kx_2/S_0)/\sigma_j, \\
\mu_A &= k_1 + k/\beta^2(M_0 - x_1/S_0), \\
\mu_{Bnj} &= k_1 - (k_{2n} - kx_2/S_0)/\sigma_j, \\
\kappa_{nj} &= k_{2n} - kx_2/S_0 + k/\beta^2(M_0 - x_1/S_0)\sigma_j.
\end{aligned} \tag{48}$$

Note that this is the far-field sound induced by the scattered pressure only. When the incident pressure is incorporated, as point out by Amiet,[18] the term 1 in the last parenthesis of Eq. 47 should be omitted, and Eq. 47 reduces to

$$\Gamma(x; \mu, \nu) = e^{-i\nu x} E(\mu x) - \sqrt{\frac{\mu}{\mu - \nu}} E((\mu - \nu)x) - \frac{1}{1 - i} e^{-i\nu x}. \tag{49}$$

3. Far field sound spectrum density

Rather than working with deterministic pressure, it is necessary to change to work with the statistical power spectrum that can be measured experimentally. The hypothetical surface pressure of frequency ω beneath a turbulent boundary layer that would exist when the trailing-edge is absent can be expressed as a Fourier integral:

$$P_{int}(\omega, x', y') = \iint P_{ia}(\omega, k_1, k_2) e^{i(k_1 x' + k_2 y')} \, dk_1 \, dk_2. \tag{50}$$

Generally, for a given fixed frequency ω, k_1 can have different values.[17] However, experiments[25] found that k_1 has a large maximum in the vicinity of ω/U_c and the convection velocity U_c is only a weak function of ω. This enables a simplification of Eq. 50 by assuming k_1 is a constant associated with frequency ω, i.e. $k_1 = \omega/U_c$. Hence, Eq. 50 reduces to

$$P_{int}(\omega, x', y') = \int_{-\infty}^{\infty} P_{ia}(\omega, k_2) e^{i(k_1 x' + k_2 y')} \, dk_2. \tag{51}$$

As shown in the preceding section, a wall pressure gust of

$$P_{ia}(\omega, k_2) e^{-i(\omega t - k_1 x' - k_2 y')}$$

will induce a far-field sound pressure of

$$\left(\frac{-i\omega x_3 c}{4\pi c_0 S_0^2} \right) \lambda \frac{\sin\left((N + 1/2)\lambda(k_2 - kx_2/S_0)\right)}{\sin\left(\lambda/2(k_2 - kx_2/S_0)\right)} \mathcal{L}(\omega, k_2) P_{ia}(\omega, k_2). \tag{52}$$

Thus, a wall pressure defined by Eq. 51 will induce a far-field sound pressure of

$$p_f(\mathbf{x}, \omega) = \left(\frac{-i\omega x_3 c}{4\pi c_0 S_0^2} \right) \int_{-\infty}^{\infty} \lambda \frac{\sin\left((N + 1/2)\lambda(k_2 - kx_2/S_0)\right)}{\sin\left(\lambda/2(k_2 - kx_2/S_0)\right)} \mathcal{L}(\omega, k_2) P_{ia}(\omega, k_2) \, dk_2. \tag{53}$$

According to Amiet,[26,17] the PSD of the far-field sound is given by

$$S_{pp} = \lim_{T \to \infty} \left(\frac{\pi}{T} \langle p_f(\mathbf{x}, \omega) p_f^*(\mathbf{x}, \omega) \rangle \right), \tag{54}$$

where $p_f^*(\mathbf{x}, \omega)$ denotes the conjugate of $p_f(\mathbf{x}, \omega)$, and $2T$ is the time length used to obtain $p_f(\mathbf{x}, \omega)$ by performing Fourier transformation. Substituting Eq. 53 into Eq. 54 yields

$$S_{pp}(\mathbf{x}, \omega) = \left(\frac{\omega x_3 c}{4\pi c_0 S_0^2} \right)^2 \int_{-\infty}^{\infty} \lambda^2 \left(\frac{\sin\left((N + 1/2)\lambda(k_2 - kx_2/S_0) \right)}{\sin\left(\lambda/2(k_2 - kx_2/S_0) \right)} \right)^2 |\mathcal{L}|^2 \, \Pi(\omega, k_2) \, \mathrm{d}k_2, \tag{55}$$

where, $\Pi(\omega, k_2)$ is the wavenumber spectral density[20] of the hypothetical surface pressure beneath the turbulent boundary layer on the airfoil surface. It is worth mentioning that if one sets the amplitude of sawtooth serrations $2h = 0$, Eq. 55 will reduce to Amiet's model.[17, 18] Eq. 55 is still rather complex, a possible simplification can be made by assuming a very large span. That is when the number of serrations $(2N + 1)$ is sufficiently large. Using the following equation:

$$\lim_{N \to \infty} \lambda^2 \frac{\sin^2\left((N + 1/2)\lambda(k_2 - kx_2/S_0) \right)}{\sin^2\left(\lambda/2(k_2 - kx_2/S_0) \right)} \sim 2\pi d \sum_{m=-\infty}^{\infty} \delta(k_2 - kx_2/S_0 + 2m\pi/\lambda), \tag{56}$$

where $\delta(x)$ is the conventional generalized function and should not be confused with the one defined in Eq. 34, one can show that the PSD of the far-field sound in the plane $y' = 0$ is given by

$$S_{pp} = \left(\frac{\omega x_3 c}{4\pi c_0 S_0^2} \right)^2 2\pi d \sum_{m=-\infty}^{\infty} |\mathcal{L}(\omega, 2\pi m/\lambda)|^2 \, \Pi(\omega, 2m\pi/\lambda). \tag{57}$$

Equation 57 is the fundamental result of this paper, and it is interesting to note that the infinite series shown in Eq. 57 appears similar to that in Howe's model shown in Eq. 71. For example, when it is assumed that the wavenumber spectral density of the surface pressure $\Pi(k_1, k_2, \omega)$ peaks only in the vicinity of $k_1 = \omega/U_c$, the leading orders of the summation terms in Eq. 71 decay quadratically with respect to the mode number m, which is the same for Eq. 57. In addition, both results show that the PSD of far-field sound is related to the wavenumber spectral density of the surface pressure through $\Pi(\omega, 2m\pi/\lambda)$, therefore a skewed wall pressure gust with $k_2 = 2m\pi/\lambda$ plays an important role in sound generation.

III.   Model validation and discussion

A.   Validation of the wall pressure gust response using FEM

1.   The FEM model

For the coupled differential equations mentioned in last section, the solutions are obtained by performing iteration procedures. The validity of such solutions can be investigated by numerically solving those equations using the Finite Element Method (FEM), which will be discussed in detail in this section. Instead of solving the far-field sound directly costing a significant amount of computational time, a feasible alternative is to calculate the near field by FEM and obtain the far-field solution by performing surface integral as adopted in analytical models.

The wave equation together with the boundary conditions given in Eqs. 5 and 4 respectively are selected to be solved. In frequency domain, these equations can be written as

$$\begin{cases} \beta^2 \dfrac{\partial^2 P}{\partial x'^2} + \dfrac{\partial^2 P}{\partial z'^2} + \dfrac{\partial^2 P}{\partial y'^2} + 2ikM_0 \dfrac{\partial P}{\partial x'} + k^2 P = 0, & \\ \dfrac{\partial P}{\partial z'}(x', y', 0) = 0, & x' < H(y') \\ P(x', y', 0) = -P_{ia} e^{i(k_1 x' + k_2 y')}, & x' \geq H(y'). \end{cases} \tag{58}$$

Note it is assumed that both x' and y' are infinite in above equations.

Computational domain   As mentioned above, the problem Eq. 58 describes is one with infinite domain, which is not practical in FEM calculations. But, a great simplification can be achieved by noting the periodic pattern of serrations. As discussed in the preceding section, the scattered pressure field on the surface of the flat plate must be periodic since the serrations are periodic in y' direction (when $k_2 \neq 0$,

the product of the scattered pressure and $e^{ik_2 y'}$ is periodic instead). This fact can thus be used in FEM computation, where the effective computational domain is reduced to only a narrow strip containing one single piece of the sawtooth serration, as shown in Fig. 5. The average chord length in the computation domain shown in Fig. 5 is $c = 1m$. The width and height of the computational domain are the wavelength of serrations λ and half of the chord length, respectively.
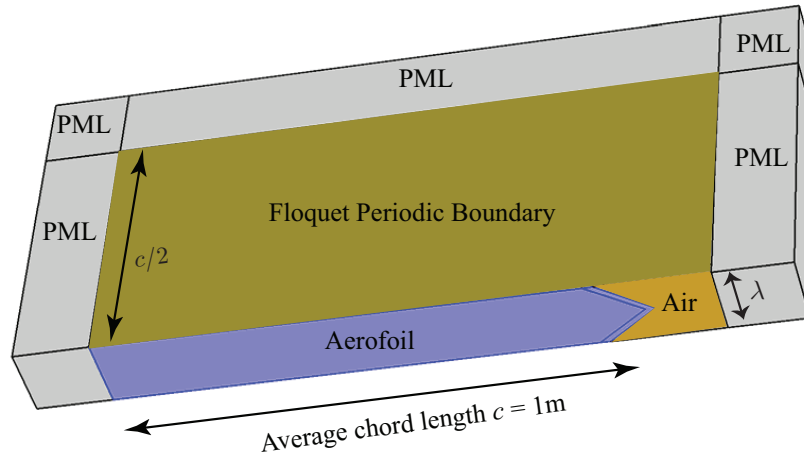

Figure 5: Illustration of the computing domain

Instead of solving Eq. 58, a pre-transformation has been made to eliminate the first-order derivative term induced by background flow. The results, of course, will be transformed back to the physical domain before comparing the FEM results and the analytical predictions.

Boundary conditions The boundary conditions are quite simple. For example, The normal velocity on the surface of the airfoil vanishes while the pressure values are fixed on the surface denoting the plane of downstream wake. In addition, as illustrated in Fig. 5, the walls on both the upper and lower sides of the computational domain represent the Floquet periodic boundary conditions. Perfectly matched layers (PMLs) have been used to avoid reflection back into the computational domain. Intuitively, it can be regarded as a layer that can perfectly absorb any incident waves, thus equivalent to an infinitely-outgoing-wave boundary.

The model set up above solves the near-field of the pressure scattered by serrated trailing-edges. The far-field sound pressure is obtained by integrating the pressure distribution on the airfoil surface. The surface pressure on the airfoil is obtained by assembling different narrow strips, each of which only contains one single piece of sawtooth. Then the following surface pressure integral is again used:

$$p_f(\mathbf{x}, \omega) = \frac{-i\omega x_3}{4\pi c_0 S_0^2} \iint_s \Delta P(x', y') e^{-ikR} \, \mathrm{d}x' \, \mathrm{d}y', \tag{59}$$

where $S_0^2 = x_1^2 + \beta^2(x_2^2 + x_3^2)$, and R takes the following form:

$$R = \frac{M_0(x_1 - x') - S_0}{\beta^2} + \frac{x_1 x' + x_2 y' \beta^2}{\beta^2 S_0}. \tag{60}$$

2. Finite element straight-edge validation

To verify that the mesh resolution is high enough to be able to capture the scattered pressure field, a straight trailing-edge case is first calculated. Fig. 6 shows the pressure distribution computed for a straight trailing-edge. It can be seen that the PMLs are good enough to simulate an infinitely-outgoing-wave boundary. The frequency used in this computation is $f = 1000$ Hz with Mach number $M_0 = 0.1$. The turbulent convection velocity is assumed $U_c = \alpha M_0 c_0$ and $\alpha = 0.7$. The wavenumbers are $k_1 = 2\pi f/U_c$, $k_2 = 0$ and the amplitude of incident wall pressure gust, P_{ia}, is unity.

In Amiet's model, the scattered pressure on the surface of the airfoil with a straight trailing-edge was found analytically by applying the Schwarzschild technique. The analytical result can thus be used to perform
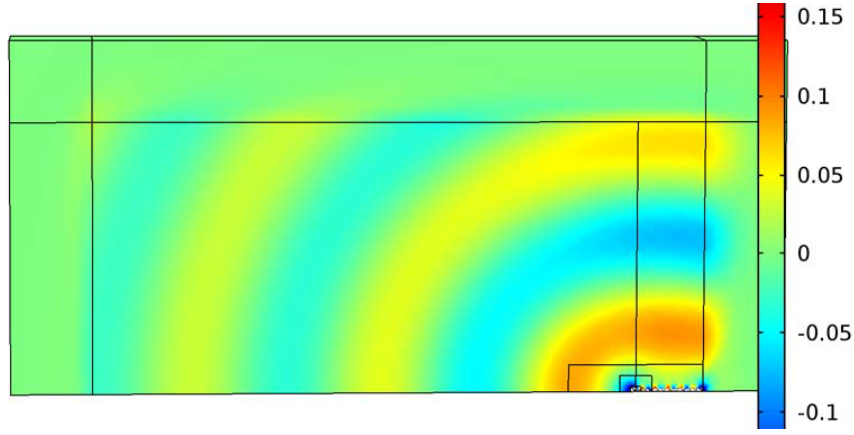
Figure 6: Computed pressure distribution scattered by a straight trailing-edge

an error analysis. It is worth noting that the FEM computation assumes a finite chord length, while the solution given by Schwarzschild's method makes use of an assumption of infinite chord. Thus, part of the discrepancy between the FEM results and the analytical model is caused by the FEM computation while the other part is due to the infinite-chord assumption in the analytical model. However, it is argued[17, 20] that the differences arising from finite chord length become increasingly small as frequency increases, which is found to be indeed this case for the validation computations. The maximum difference at $f = 1000$ Hz including the computational and systematic errors is found to be under 1%.

3. Comparison between the model and FEM computation

This section presents a direct comparison between the gust-induced far-field sound pressure, i.e. Eq. 43 and FEM simulations. The far-field sound pressure induced by a wall pressure gust of $k_2 = 0$ at different frequencies is chosen for comparison. It can be found that a sound reduction of more than 20 dB can be achieved for the far-field sound induced by this specific wall pressure gust. The surface pressure under turbulent boundary layer, however, comprises different wall pressure gust components, each of which has a different value of k_2. Thus the aforementioned sound reduction must not be confused with the overall sound reduction of the real trailing-edge noise, which is induced by the surface pressure under the turbulent boundary layer, rather than a single wall pressure gust component. Note that in the mathematical model, we only use the first-order approximation, i.e. the gust-response function $\mathcal{L}$ takes the following form:

$$\mathcal{L}(\omega, k_2) \approx (1 - i) \frac{1}{\lambda c} \left(\sum_{n'=-\infty}^{\infty} \left(\Theta_{n'} + \Theta_{n'}^{(1)} \right) \right) e^{-ik/\beta^2 (M_0 x_1 - S_0)} e^{ik/\beta^2 (M_0 - x_1/S_0)h}. \tag{61}$$

The chord length c is chosen to be unity with a span-to-chord ratio of 8. It is assumed that $k_1 = \omega/U_c$ and the convection speed U_c is taken to be $0.7U$. The Mach number and geometrical shape of the serrations can vary in different cases.

Results will be presented for a range of wide to sharp serrations, see Figs. 7 through 9. It is interesting to note that for large Mach numbers, no significant sound reduction is achieved at frequencies of interest.[27] Thus, we shall only focus on the low Mach numbers, i.e. $M_0 \leq 0.2$. The far-field SPL, i.e. $20 \log_{10} |p_f(\mathbf{x}, \omega)|$, obtained from the FEM model at 90° above the trailing-edge in the mid-span plane with $x_3 = 1$, is plotted against theoretical predictions. Results are provided for both the baseline (no serration, i.e. $h = 0$) and the serrated trailing-edge.

In Fig. 7a, the serration used is $\lambda/h = 6, h/c = 0.025$ while Mach number is 0.1. For the baseline, the comparison of the theoretical model against the FEM model shows that an overall good agreement is achieved over the frequency range of interest. The deviation occurring at low frequencies is due to the finite chord effect. It can be also seen that as the frequency increases, the deviation becomes progressively less pronounced. Results obtained for the serrated trailing-edge, on the other hand, show that the theoretical results follow the general trend of the FEM results fairly accurately, which suggests that the analytical model can capture the essential physics and provide accurate predictions.

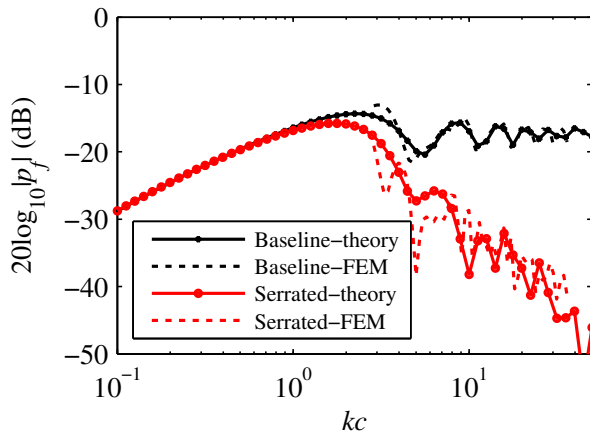American Institute of Aeronautics and Astronautics
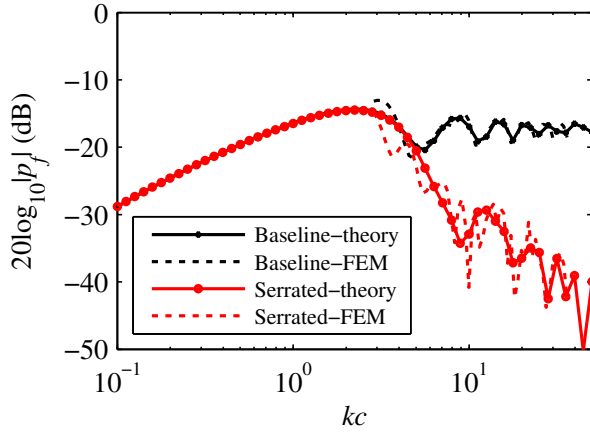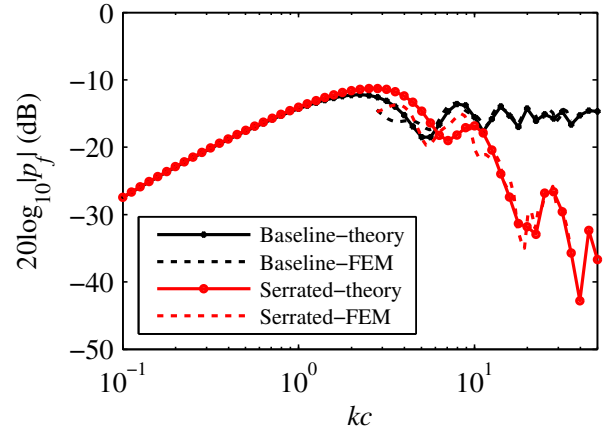
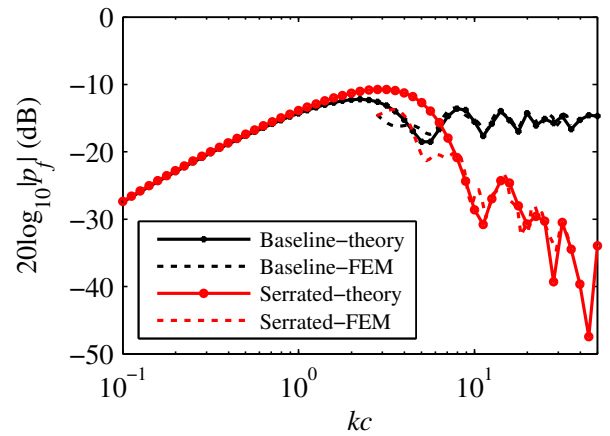(a) $M_0 = 0.1$　　　　　　　　　　　(b) $M_0 = 0.2$

Figure 7: SPL at 90° above the trailing-edge in the mid-span plane with $x_3 = 1$ due to a wall pressure gust of frequency ω with $k_2 = 0$, parameters of the serrations are $\lambda/h = 6, h/c = 0.025$.

(a) $M_0 = 0.1$　　　　　　　　　　　(b) $M_0 = 0.2$

Figure 8: SPL at 90° above the trailing-edge in the mid-span plane with $x_3 = 1$ due to a wall pressure gust of frequency ω with $k_2 = 0$, parameters of the serrations are $\lambda/h = 3, h/c = 0.05$.

American Institute of Aeronautics and Astronautics

In Fig. 7b, the far-field SPL for the same serrated sawtooth trailing-edge but at $M_0 = 0.2$ is plotted. Generally, the FEM computation at higher Mach numbers can be expected to be more precise than that at low Mach numbers. This is due to the fact that the hydrodynamic wavenumber k_1 is given by $k/(\alpha M_0)$, and a smaller k_1 improves the spatial resolution of the mesh. As can be seen in Fig. 7b, an excellent agreement for baseline results is obtained. For serrated trailing-edges, the agreement is good and trends are captured quite accurately.

Fig. 8a and Fig. 8b present the far-field SPL for serrations of $\lambda/h = 3, h/c = 0.05$ at $M_0 = 0.1$ and $M_0 = 0.2$, respectively. Except at low frequencies where the finite chord length issue plays a role in causing errors in the FEM simulations, the theory generally agrees well with the FEM results.

The serrations studied here are not normally considered as sharp enough to reduce the trailing-edge noise significantly.[6] Figure 9a and Fig. 9b show the results for serrations of $\lambda/h = 1, h/c = 0.05$ at $M_0 = 0.1$ and $\lambda/h = 0.6, h/c = 0.05$ at $M_0 = 0.1$, respectively. It can be seen from these two figures that for sharper serrations, the average error between numerical calculations and theoretical predictions normally increases, which might have been caused by the convergence rate of the first-order approximation used. The trends are, however, very similar to the FEM results.
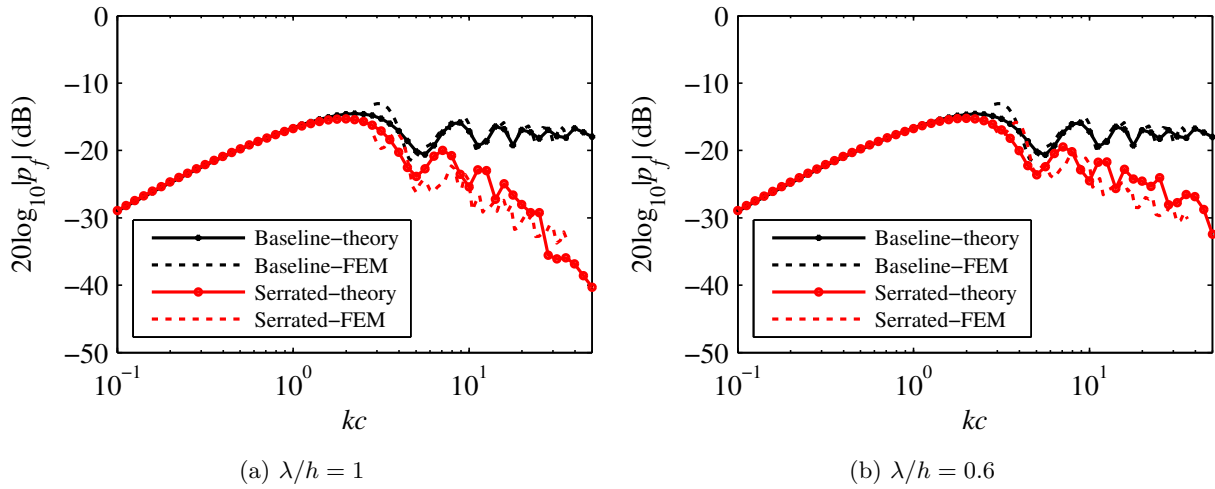

(a) $\lambda/h = 1$ (b) $\lambda/h = 0.6$

Figure 9: SPL at $90°$ above the trailing-edge in the mid-span plane with $x_3 = 1$ due to a wall pressure gust of frequency ω with $k_2 = 0$, parameters of the serrations are $h/c = 0.05$ with Mach number $M_0 = 0.1$.

B. Discussion on the effects of serration geometry

As demonstrated in the preceding section, under the large span assumption, Eq. 57 can accurately predict the far-field sound PSD. This equation, however, can be further simplified if the serration is sufficiently sharp such that $\Pi(\omega, 2\pi/\lambda) \ll \Pi(\omega, 0)$, then

$$S_{pp} = \left(\frac{\omega x_3 c}{4\pi c_0 S_0^2} \right)^2 2\pi d \left| \mathcal{L}(\omega, 0) \right|^2 \Pi(\omega, 0). \tag{62}$$

Performing an inverse Fourier transformation on the wavenumber spectral density function $\Pi(\omega, k_2)$ gives the cross-spectral density of $S_{qq}(\omega, y')$, consequently

$$\Pi(\omega, 0) = \frac{1}{2\pi} \int_{-\infty}^{\infty} S_{qq}(\omega, y') \, \mathrm{d}y'. \tag{63}$$

Equivalently, the far field PSD function S_{pp} can be written as

$$S_{pp} = \left(\frac{\omega x_3 c}{4\pi c_0 S_0^2} \right)^2 l_{y'}(\omega) d \left| \mathcal{L}(\omega, 0) \right|^2 S_{qq}(\omega, 0), \tag{64}$$

American Institute of Aeronautics and Astronautics

where the correlation length in the y' direction is defined as

$$l_{y'}(\omega) = \frac{1}{S_{qq}(\omega,0)} \int_{-\infty}^{\infty} S_{qq}(\omega, y') \, \mathrm{d}y'. \tag{65}$$

For the case of wide serrations, the higher-order summation in Eq. 57 can not be dropped. But note that $|\mathcal{L}(\omega, 2m\pi/\lambda)|^2 > 0$, and that the less modes to be summed in Eq. 57, the smaller the value of S_{pp} is. Thus one condition for an efficient trailing-edge sound reduction is that $\Pi(\omega, 2m\pi/\lambda) \ll \Pi(\omega, 0)$ for $m > N_0$ where N_0 is an integer but sufficiently small such that Eq. 57 still yields a smaller value than that of a straight trailing-edge. It can be shown in the following sections that this condition can be equivalently stated as that the non-dimensional parameter $k_1 l_{y'}(\omega)\sigma \gg 1$.

To further estimate the value of S_{pp} in this case, a detailed investigation of the gust-response function $\mathcal{L}$ is needed. Careful examination of Eq. 44 shows that $|\mathcal{L}|^2$ is proportional to the value of $1/|\kappa_{n'j}|^2$, thus one can expect that the value of $|\mathcal{L}|^2$ is dominated by the mode n where $\kappa_{nj} \approx 0$, i.e.

$$|\mathcal{L}|^2 \approx \frac{2}{\lambda c} \left| a_n Q_{nn} + \Theta_n^{(1)} + \Theta_n^{(2)} + \cdots \right|^2. \tag{66}$$

By further noting that $\alpha_{n'm} = 4h/(\pi^2(n'-m)^2)$ for $n'-m = odd$, $\Theta_n^{(i)}$ may be approximated by only summing over mode $n-1$ and $n+1$. Therefore, for fixed serration geometry, increasing frequency reduces the value of $|a_n|$ and thus reduce the value of $|\mathcal{L}|^2$. From the definition of a_n in Eq. 20, it can be shown that a small value of $|a_n|$ can be achieved by ensuring the non-dimensional parameter $k_1 h \gg 1$. Thus another condition for achieving significant trailing-edge reduction is to ensure that $k_1 h$ is sufficiently large.

IV.   Model results

This section presents results of the new model based on Eq. 57. For illustration purpose, we adopt Chase's model[28] of the wavenumber spectral density. It is argued by Chase[28] that the convection velocity U_c is weakly dependent on frequency, and on average $U_c \approx 0.7U$ and the wavenumber spectral density is well approximated by

$$\frac{C_m \rho_0^2 v_*^3 k_1^2 \delta^5}{((k_1 - \omega/U_c)^2 (\delta U_c/3v_*)^2 + (k_1^2 + k_2^2)\delta^2 + \chi^2)^{5/2}}, \tag{67}$$

where, ρ_0 and δ are the fluid density and the boundary layer thickness respectively, $C_m \approx 0.1553, \chi \approx 1.33, v_* \approx 0.03U$. Clearly, this function only obtains a large value in the vicinity of the region centered on $k_1 = \omega/U_c$. Here we assume k_1 is always ω/U_c and obtain $\Pi(\omega, k_2)$ by integrating Eq. 67 with respect to k_1 and then keeping the leading order terms,[11] which yields

$$\Pi(\omega, k_2) \approx \frac{4C_m \rho_0^2 v_*^4 (\omega/U_c)^2 \delta^4}{U_c \left(((\omega/U_c)^2 + k_2^2)\delta^2 + \chi^2\right)^2}. \tag{68}$$

Substituting the formula presented in Eq. 68 into Eq. 57 and using $(\rho_0 v_*^2)^2 (d/c_0)$[11] to non-dimensionalize the far field PSD yields

$$\frac{S_{pp}(\mathbf{x}, \omega)}{(\rho_0 v_*^2)^2 (d/c_0)} = \frac{C_m}{2\pi} \Psi(\mathbf{x}, \omega), \tag{69}$$

where, function $\Psi(\mathbf{x}, \omega)$ is defined as

$$\Psi(\mathbf{x}, \omega) = \left(\frac{x_3 c}{S_0^2}\right)^2 \frac{U_0}{c_0} \sum_{m=-\infty}^{\infty} |\mathcal{L}(\omega, 2\pi m/\lambda)|^2 \frac{(\omega\delta/U_c)^4}{\left(((\omega\delta/U_c)^2 + (2m\pi\delta/\lambda)^2) + \chi^2\right)^2}. \tag{70}$$

The following figures are plotted using Eq. 70 by varying λ and h. As discussed above, we shall only focus on low Mach numbers, i.e. $M_0 \leq 0.2$. The function $\mathcal{L}$ in Eq. 70 is defined in Eq. 44 and we take the first-order approximation here. Note that the incident pressure is also taken into consideration (leaving out 1 in Eq. 47, see Amiet[18]). The observer point is at 90° above the trailing edge in the mid-span plane, namely $(x_1 = 0, x_2 = 0, x_3 = 1)$. The normalized power spectrum for serrations of an edge of slope $4h/\lambda = 0.5$ is shown in Fig. 10a. The sound reduction is approximately zero over the entire the frequency range of interest.

In Fig. 10b, the serrations have quite a large wavelength λ and the slope in this case is $4h/\lambda = 1$. No noise reduction is achieved at low frequencies, i.e. $kc < 2$, and a noise reduction of about 5 dB is obtained at high frequencies.

Fig. 11a shows the result for $4h/\lambda = 2$. As can be seen, this type of serrations gives better sound reduction performance than in the previous case. Further decreasing the wavelength λ will result in more sound reduction, as presented in Fig. 11b. For sharp serrations, significant sound reduction is achieved at both low and high frequencies, as presented in Fig. 12a, in which case the slope is $4h/\lambda = 10$.
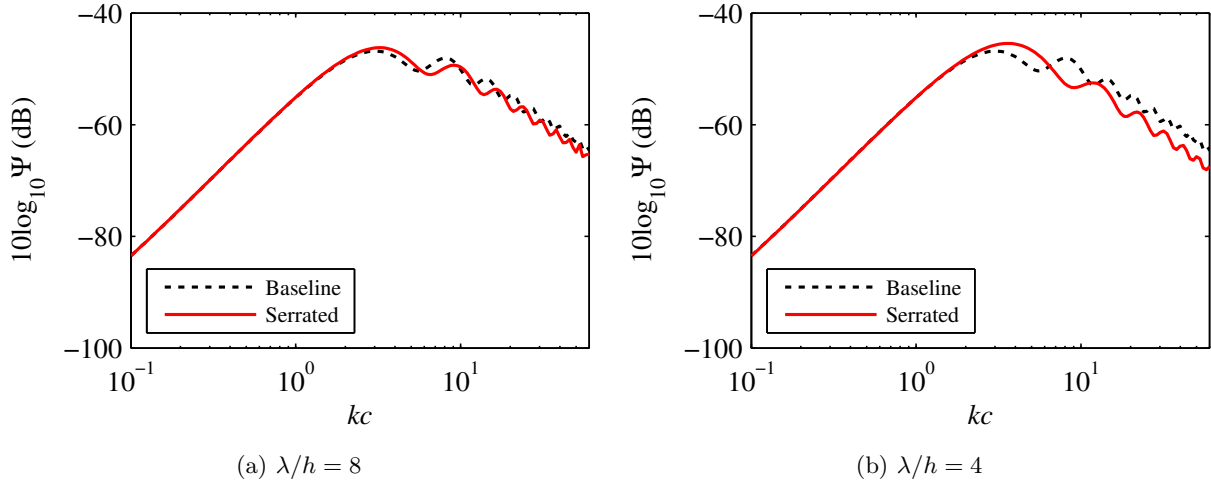

(a) $\lambda/h = 8$ (b) $\lambda/h = 4$

Figure 10: The normalized spectrum for straight and serrated trailing-edges, $h/c = 0.025, M_0 = 0.1$, the observer is at $90°$ above the trailing-edge in the mid-span plane with $x_3 = 1$.
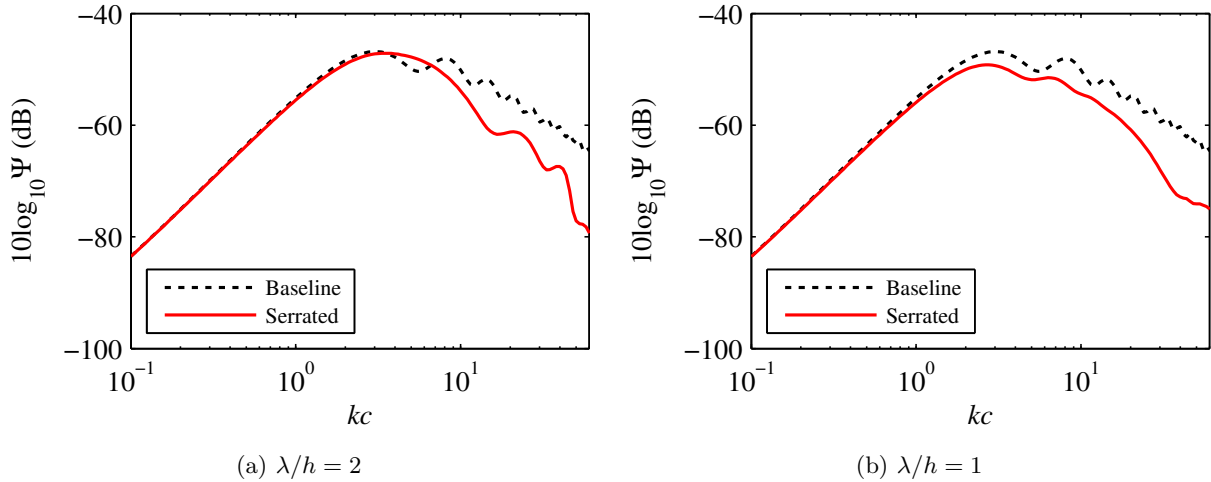

(a) $\lambda/h = 2$ (b) $\lambda/h = 1$

Figure 11: The normalized spectrum for straight and serrated trailing-edges, $h/c = 0.05, M_0 = 0.1$, the observer is at $90°$ above the trailing-edge in the mid-span plane with $x_3 = 1$.

Another interesting fact is that when the serrations are sharp enough, i.e. $\lambda/h < 0.4$, further decreasing the wavelength of serration has no effect on the sound reduction at low frequencies, e.g. $kc < 10$, and only improves the noise reduction performance at high frequencies. The result obtained for a sawtooth serration with $\lambda/h = 0.2, h/c = 0.05$ at $M_0 = 0.1$ is shown in Fig. 12b. Comparing Fig. 12a and Fig. 12b suggests that a better performance for sound reduction is achieved at high frequencies while no difference can be observed at frequencies of $kc < 10$.
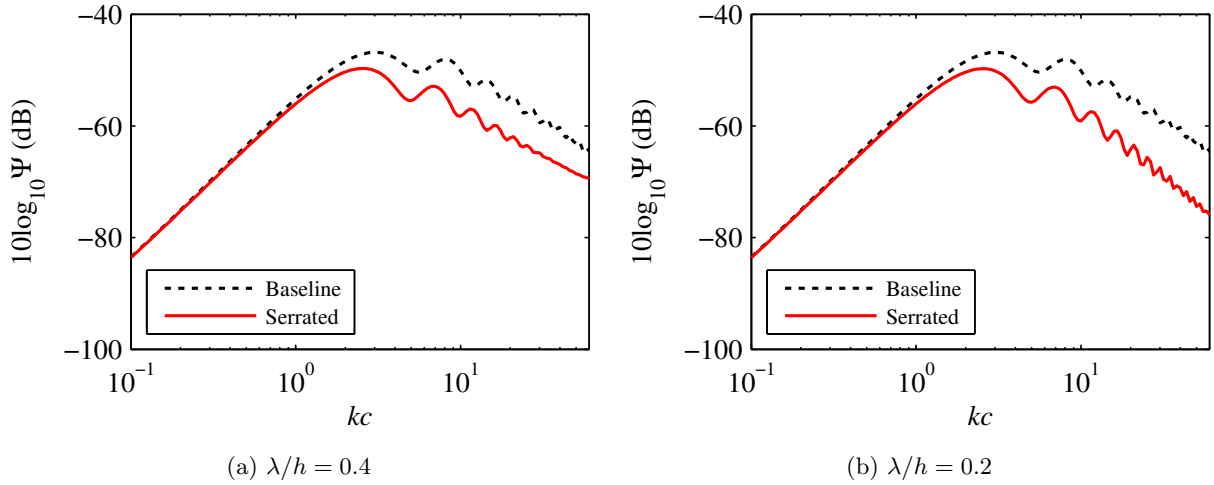
American Institute of Aeronautics and Astronautics

(a) $\lambda/h = 0.4$ (b) $\lambda/h = 0.2$

Figure 12: The normalized spectrum for straight and serrated trailing-edges, $h/c = 0.05, M_0 = 0.1$, the observer is at $90°$ above the trailing-edge in the mid-span plane with $x_3 = 1$.

V. Comparison with Howe's model

As mentioned earlier, the aim of this paper is to find a more accurate model to predict the far-field sound generated by serrated trailing-edges. To compare with Howe's model, the results obtained by Howe for a trailing-edge with sawtooth serrations are briefly listed here.

The model considered by Howe is illustrated in Fig. 3. The observer point has a fly-over angle θ and an angle ϕ as define in Fig. 3. To simplify the model, Howe assumes

- The statistical property of the turbulence inside the boundary layer remains the same before and after passing the trailing-edge;

- The Mach number is sufficiently low to neglect the convection effect;

- The Green's function can be approximated by modifying the Green's function for the sound diffraction by a straight trailing-edge and the slender wing approximation continues to be valid for sharp serrations.

Adopting these assumptions and Chase's model for the turbulent boundary layer wavenumber spectrum, Howe shows that the far-field sound power spectrum at the observer point can be expressed as

$$\frac{S_{pp}(\omega, \mathbf{x})}{(\rho_0 v_*^2)^2 (d/c_0)(\delta/|\mathbf{x}|)^2} = C_m/\pi \sin^2(\theta/2) \sin(\phi) \Psi_f(\omega), \tag{71}$$

where,

$$\Psi_f(\omega) = 8(h/\delta)^2 \sum_{n=-\infty}^{\infty} \frac{(\omega h/U_c)^2 [(\omega h/U_c)^2 + (2n\pi h/\lambda)^2][1 - \cos(2\omega h/U_c)/\cos(n\pi)]}{[(2\omega h/U_c)^2 - n^2\pi^2]^2 [(\omega h/U_c)^2 + (2n\pi h/\lambda)^2 + (\chi h/\delta)^2]^2}. \tag{72}$$

where, ρ_0 denotes the fluid density, δ represents boundary layer thickness, and $C_m \approx 0.1553, \chi \approx 1.33$ and $v_* \approx 0.03U$ are the values used in Chase's model for the wave-number frequency spectrum.

Even thought the assumption of frozen turbulence is used in both models, Howe's model differs from the model presented in this paper in several ways. In Howe's model, the far-field sound pressure is obtained by making use of a Green's function for sound diffraction by an edge. This Green's function is obtained by making use of a modified Green's function for a straight trailing-edge and the slender wing approximation. The model developed in this paper, however, gives the scattered sound by solving the convected wave equation. Howe's model neglects the effects of convection, so it is only valid at low Mach numbers. The
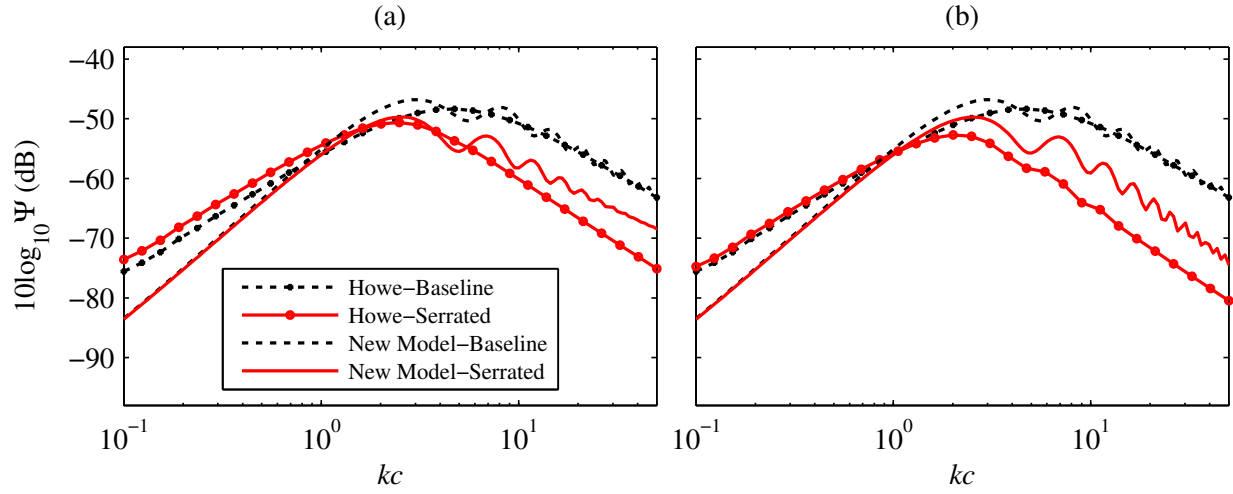
Figure 13: The normalized spectrum of Howe's model and the new model, $h/c = 0.05$, $M_0 = 0.1$, the observer is at $90°$ above the trailing-edge in the mid-span plane with $x_3 = 1$. (a)$\lambda/h = 0.4$, $h/c = 0.05$, $M_0 = 0.1$ (b) $\lambda/h = 0.2$, $h/c = 0.05$, $M_0 = 0.1$

new model is valid for any Mach numbers, as the convection effects have been incorporated in the convected wave equation.

Figures in this section represent the results obtained by normalizing Howe's model, i.e. Eq. 71, and the model developed in this paper, i.e. Eq. 69. The normalized spectrum $\Psi(\mathbf{x}, \omega)$ is defined the same as in Eq. 69. The result of the new model is obtained by taking the effects of incident wall pressure gust into consideration (leaving out 1 in Eq. 47), which, according to Amiet,[18] systematically increases the noise level by 6 dB. As can be seen from Fig. 13(a), the comparison of the results shows a clear difference between the two methods. The serration used in Fig. 13(a) has $\lambda/h = 0.4$, $h/c = 0.05$ and the Mach number $M_0 = 0.1$. At high frequencies, i.e. $kc \approx 50$, Howe's model gives a sound reduction of about 13 dB and the new model gives about 7 dB. Fig. 13(b) presents the comparison for shaper serrations: $\lambda/h = 0.2$, $h/c = 0.05$ at $M_0 = 0.1$. At the frequency of $kc \approx 50$, the noise reduction predicted by Howe's model and the new model are, respectively, 18 dB and 10 dB. Generally, the new model gives less sound reduction than Howe's model, and can thus give better agreement with experiments.

VI. Noise reduction mechanism

As shown in Sec. III.B, the noise reduction performance is believed to depend on two main non-dimensional parameters, $k_1 h$ and $k_1 l_{y'}(\omega)\sigma$. In this section, we will discuss the two parameters, and attempt to understand the implied physics.

With regard to the condition that $k_1 h \gg 1$, it can be readily shown by evaluating Eq. 20 that $|a_n|$ decreases as $k_1 h$ increases. Therefore, for a fixed serration geometry high frequencies are preferable in terms of noise reduction. This also means that the root-to-tip length determines the effective frequency range where sound reduction can be achieved. For small h, the frequency range shifts towards high frequencies. It is straightforward to understand its physical meaning. When focusing on the edge of a specific sawtooth, one finds that the scattered near-field pressures on different segments of one single edge have different phases. As the observer is in the far-field and the spatial range of those phase differences is always small compared to the wavelength of sound, the far-field sound generated by different segments tend to cancel each other. And the higher the frequencies are, the more effective the cancellation is. This explains why $k_1 h \gg 1$ is required to ensure significant sound reduction can be achieved, namely, creating enough phase difference.

Regarding the parameter $k_1 l_{y'}(\omega)\sigma$, we have mentioned in Sec. III.B that the condition $k_1 l_{y'}(\omega)\sigma \gg 1$ implies $\Pi(\omega, 2m\pi/\lambda) \ll \Pi(\omega, 0)$ for $m > N_0$. This can be made clear by noting

$$\Pi(\omega, \frac{2m\pi}{\lambda}) = \frac{1}{2\pi} \int_{-\infty}^{\infty} S_{qq}(\omega, y') e^{-i\frac{2m\pi}{\lambda}y'} \, \mathrm{d}y'. \tag{73}$$

American Institute of Aeronautics and Astronautics

When $k_1 l_{y'}(\omega)\sigma = 4k_1 h l_{y'}(\omega)/\lambda \approx N_0 l_{y'}(\omega)/\lambda \gg 1$, the integrand in Eq. 73 oscillates rapidly within the length scale of $S_{qq}(\omega, y')$, and the integral obtains a small value compared to the value of $\Pi(\omega, 0)$ as a result of destructive interference. Note that the root-to-tip length $2h = \sigma\lambda/2$, we can define an effective root-to-tip length as $2h_e = \sigma l_{y'}(\omega)$. The effective length $2h_e$ therefore means the equivalent root-to-tip length where the turbulence can be deemed as coherent. Therefore the far-field sound can be reduced if $k_1 h_e \gg 1$. Physically, this means those phase differences should be well situated in a correlated turbulent structure, an eddy for example. Otherwise, the phase differences induced are not "real" phase differences, in the sense that they are not "fully correlated". This can be made clear when one considers a limit case, e.g. when the spanwise correlation length is zero: the scattered pressure on every segment of an edge is statistically independent, so no cancellation is possible.

VII. Conclusion

A new mathematical model is developed in this paper in the aim to predict the sound radiated by serrated trailing-edges more accurately. By making use of the Fourier expansion and the Schwarzschild techniques, the PSD of far-field sound is related to the wavenumber spectral density of the hypothetical wall pressure beneath the turbulent boundary layer that would exist when the trailing-edge is absent using Amiet's approach.[18] It has been found that the new model can predict the sound reduction better than Howe's model.[11,7] According to the new model, the sound reduction achieved by a trailing-edge with sharp sawtooth serrations is around 5-10 dB for a wide bandwidth. This result can better agree with prior experimental observations, in which the average sound reduction is reported to be 5-7 dB.[6]

It is found that the physical mechanism of sound reduction by using serrations is the destructive interference effect due to the out-of-phased scattered pressure in the vicinity of the trailing-edge. Two geometrical parameters are found critical in determining the sound reduction. First, the root-to-tip length needs to satisfy $k_1 h \gg 1$ to ensure sufficient phase differences are induced along the edge. Second, the value of $k_1 h_e \gg 1$ is required to ensure the phase differences induced as above are "fully correlated". For the boundary layer flow above a flat plate, this can be equivalently expressed as the slope $4h/\lambda$ of the sawtooth edges should be large enough. The sound reduction generally increases as the slope increases. But if the serrations are already sharp enough, further increasing the slope only affects high frequencies.

The results obtained using the new model agree well with FEM computations, suggesting the model developed in this paper can capture the essential physics and give correct predictions for the sound generated by serrated trailing-edges.

Appendix

A.   Second iterated results

The solution after second iteration, can be expressed as,

$$\mathbf{P}^{(2)}(x,0) = \mathbf{N}(x) + \mathbf{C}^{(1)}(x) + \mathbf{C}^{(2)}(x), \tag{74}$$

where, $\mathbf{N}(x)$ and $\mathbf{C}^{(1)}(x)$ are defined in Sec. II, and $\mathbf{C}^{(2)}(x)$ whose entry corresponding to mode n' is

$$
\begin{aligned}
C_{n'}^{(2)}(x) =& P_{ia}(1-i)\mathrm{e}^{\mathrm{i}k_1 x} \sum_{m=-\infty}^{\infty} \left\{ \beta_{n'm}(\mathrm{i}k_1)^2 (\mathrm{E}(-\mu_{n'}x) - \mathrm{E}(-\mu_m x)) \right. \\
& - \left(\beta_{n'm}\mathrm{i}k_1 + \gamma_{n'm}\mathrm{i}(k_1 - \mu_m)\right)\sqrt{\frac{\mu_m}{-2\pi x}}(\mathrm{e}^{-\mathrm{i}\mu_{n'}x} - \mathrm{e}^{-\mathrm{i}\mu_m x}) \\
& \left. - \frac{\gamma_{n'm}}{2}\left(\sqrt{\frac{\mu_m}{-2\pi x}}\frac{1}{(-x)}(\mathrm{e}^{-\mathrm{i}\mu_{n'}x} - \mathrm{e}^{-\mathrm{i}\mu_m x}) - \mathrm{i}(\mu_{n'} - \mu_m)\sqrt{\frac{\mu_m}{-2\pi x}}\mathrm{e}^{-\mathrm{i}\mu_{n'}x}\right) \right\}
\end{aligned} \tag{75}
$$

where,

$$\beta_{ln} = \sum_{m=-\infty}^{\infty}\left(\alpha_{ln}a_m - B_{lm}/(k_{2l}^2 - k_{2n}^2)a_n\right)\alpha_{nm},$$

$$\gamma_{ln} = \sum_{m=-\infty}^{\infty}\left(\alpha_{ln}a_m\sqrt{\mu_m/\mu_n} - B_{lm}/(k_{2l}^2 - k_{2n}^2)a_n\right)\alpha_{nm},$$

The function T_{nm} involved in the second iteration can be further defined similarly,

$$
\begin{aligned}
T_{nm} = \sum_{j=0}^{1} \frac{1}{\mathrm{i}\kappa_{nj}} \Bigg\{ &\left(\frac{\mathrm{i}\eta_{Am}}{\sqrt{\eta_{Am}}} \big(\mathrm{e}^{\mathrm{i}\kappa_{nj}\lambda_{j+1}} \mathrm{E}(\eta_{Am}(c+\epsilon_{j+1})) - \mathrm{e}^{\mathrm{i}\kappa_{nj}\lambda_j} \mathrm{E}(\eta_{Am}(c+\epsilon_j)) \big) \right. \\
&- \frac{\mathrm{i}\eta_{Bmj}}{\sqrt{\eta_{Bmj}}} \mathrm{e}^{\mathrm{i}\kappa_{nj}(\lambda_j-(c+\epsilon_j)/\sigma_j)} \big(\mathrm{E}(\eta_{Bmj}(c+\epsilon_{j+1})) - \mathrm{E}(\eta_{Bmj}(c+\epsilon_j)) \big) \Big) - \\
&\left(\big(\mathrm{e}^{\mathrm{i}\kappa_{nj}\lambda_{j+1}} \frac{1}{\sqrt{2\pi(c+\epsilon_{j+1})}} \mathrm{e}^{\mathrm{i}\eta_{Am}(c+\epsilon_{j+1})} - \mathrm{e}^{\mathrm{i}\kappa_{nj}\lambda_j} \frac{1}{\sqrt{2\pi(c+\epsilon_j)}} \mathrm{e}^{\mathrm{i}\eta_{Am}(c+\epsilon_j)} \big) \right. \\
&\left. \left. - \mathrm{e}^{\mathrm{i}\kappa_{nj}(\lambda_j-(c+\epsilon_j)/\sigma_j)} \big(\frac{1}{\sqrt{2\pi(c+\epsilon_{j+1})}} \mathrm{e}^{\mathrm{i}\eta_{Bmj}(c+\epsilon_{j+1})} - \frac{1}{\sqrt{2\pi(c+\epsilon_j)}} \mathrm{e}^{\mathrm{i}\eta_{Bmj}(c+\epsilon_j)} \big) \right) \right\},
\end{aligned}
\tag{76}
$$

The 2nd iterated solution falls into the same pattern,

$$
\begin{aligned}
p^{(2)}(\mathbf{x},\omega) = &\frac{-\mathrm{i}\omega x_3}{2\pi c_0 S_0^2} P_{ia} \mathrm{e}^{-\mathrm{i}k/\beta^2(Mx_1-S_0)} \mathrm{e}^{\mathrm{i}k/\beta^2(M-x_1/S_0)h}(1-\mathrm{i}) \\
&\frac{\sin\big((N+1/2)\lambda(k_2-kx_2/S_0)\big)}{\sin\big(\lambda/2(k_2-kx_2/S_0)\big)} \sum_{n'=-\infty}^{\infty} \left(\Theta_{n'} + \Theta_{n'}^{(1)} + \Theta_{n'}^{(2)} \right)
\end{aligned}
\tag{77}
$$

where, $\Theta_{n'}$ and $\Theta_{n'}^{(1)}$ are defined in Sec. II, and

$$
\begin{aligned}
\Theta_{n'}^{(2)} = \sum_{m=-\infty}^{\infty} &\beta_{n'm}(\mathrm{i}k_1)^2(Q_{n'n'}-Q_{n'm}) - (\beta_{n'm}\sqrt{\mu_m}\mathrm{i}k_1 + \gamma_{n'm}\sqrt{\mu_m}\mathrm{i}(k_1-\mu_m))(S_{n'n'}-S_{n'm}) \\
&- \gamma_{n'm}\sqrt{\mu_m}\big(T_{n'n'}-T_{n'm}-\mathrm{i}/2(\mu_{n'}-\mu_m)S_{n'n'}\big)
\end{aligned}
\tag{78}
$$

Acknowledgments

References

[1] Casalino, D., Diozzi, F., Sannino, R., and Paonessa, A., "Aircraft noise reduction technologies: a bibliographic review," *Aerospace Science and Technology*, Vol. 12, Jan. 2008, pp. 1–17.

[2] Pedersen, E. and Waye, K. P., "Perception and annoyance due to wind turbine noise – a dose-response relationship," *The Journal of the Acoustical Society of America*, Vol. 116, No. 6, 2004, pp. 3460–3470.

[3] Chase, D. M., "Noise radiated from an edge in turbulent flow," *AIAA journal*, Vol. 13, Aug. 1975, pp. 1041–1047.

[4] Williams, J. E. F. and Hall, L. H., "Aerodynamic sound generation by turbulent flow in the vicinity of a scattering half plane," *Journal of Fluid Mechanics*, Vol. 40, March 1970, pp. 657–670.

[5] Parchen, R., Hoffmans, W., Gordner, A., and Braun, K., "Reduction of airfoil self-noise at low Mach number with a serrated trailing edge," *International Congress on Sound and Vibration, 6th Technical Univ of Denmark, Lyngby, Denmark*, 1999, pp. 3433–3440.

[6] Gruber, M., *Airfoil noise reduction by edge treatments*, Ph.D. thesis, 2012.

[7] Howe, M. S., "Aerodynamic noise of a serrated trailing edge," *Journal of Fluids and Structures*, Vol. 5, 1991, pp. 33–45.

[8] Ver, I. L., "Noise of jet engine test cells," *Jet Engine Test Cell Meeting*, 1987.

[9] Arndt, R. E. A. and Nagel, R. T., "Effects of leading edge serrations on noise radiation from a model rotor," *AIAA paper 72-655*, 1972.

[10] Hersh, A. S., Sodermant, P. T., and Hayden, R. E., "Investigation of acoustic effects of leading-edge serrations on airfoils," *Journal of Aircraft*, Vol. 11, 1974, pp. 197–202.

[11] Howe, M. S., "Noise produced by a sawtooth trailing edge," *The Journal of the Acoustical Society of America*, Vol. 90, 1991, pp. 482–487.

[12] Azarpeyvand, M., Gruber, M., and Joseph, P. F., "An analytical investigation of trailing edge noise reduction using novel serrations," *19th AIAA/CEAS Aeroacoustics Conference*, Aeroacoustics Conferences, American Institute of Aeronautics and Astronautics, May 2013.

[13]Dassen, A. G. M., Parchen, R., Bruggeman, J., and Hagg, F., "Results of a wind tunnel study on the reduction of airfoil self-noise by the application of serrated blade trailing edges," *Proceeding of the European Union Wind Energy Conference and Exhibition*, 1996, pp. 800–803.

[14]Oerlemans, S., Fisher, M., Maeder, T., and Kögler, K., "Reduction of wind turbine noise using optimized airfoils and trailing-edge serrations," *AIAA journal*, Vol. 47, 2009, pp. 1470–1481.

[15]Callender, B., Gutmark, E. J., and Martens, S., "Far-field acoustic investigation into chevron nozzle mechanisms and trends," *AIAA Journal*, Vol. 43, No. 1, Jan. 2005, pp. 87–95.

[16]Yan, J., Panek, L., and Thiele, F., "Simulation of jet noise from a long-cowl nozzle with serrations," *13th AIAA/CEAS Aeroacoustics Conference (28th AIAA Aeroacoustics Conference)*, Aeroacoustics Conferences, American Institute of Aeronautics and Astronautics, May 2007.

[17]Amiet, R. K., "Noise due to turbulent flow past a trailing edge," *Journal of Sound and Vibration*, Vol. 47, No. 3, 1976, pp. 387–393.

[18]Amiet, R. K., "Effect of the incident surface pressure field on noise due to turbulent flow past a trailing edge," *Journal of Sound and Vibration*, Vol. 57, 1978, pp. 305–306.

[19]Landahl, M., *Unsteady Transonic Flow*, Pergamon Press, Inc, New York, 1961.

[20]Roger, M. and Moreau, S., "Back-scattering correction and further extensions of Amiet's trailing-edge noise model. Part 1: theory," *Journal of Sound and Vibration*, Vol. 286, Sept. 2005, pp. 477–506.

[21]Roger, M. and Carazo, A., "Blade-geometry considerations in analytical gust-airfoil interaction noise models," *16th AIAA/CEAS Aeroacoustics Conference*, 2010, pp. 1–17.

[22]Curle, N., "The influence of solid boundaries upon aerodynamic sound," *Proceedings of the Royal Society A: Mathematical, Physical and Engineering Sciences*, Vol. 231, Sept. 1955, pp. 505–514.

[23]Roger, M., Schram, C., and Santana, L. D., "Reduction of airfoil turbulence-impingement noise by means of leading-edge serrations and/ or porous materials," *19th AIAA/ CEAS Aeroacoustics Conference*, 2013, pp. 1–20.

[24]Süli, E. and Mayers, D., *An introduction to numerical analysis*, Cambridge University Press, 2003.

[25]Willmarth, W. W., "Space-time correlations and spectra of wall pressure in a turbulent boundary layer," *NASA Tech Memo 3-17-59W*, 1959.

[26]Amiet, R. K., "Acoustic radiation from an airfoil in a turbulent stream," *Journal of Sound and Vibration*, Vol. 41, No. 4, 1975, pp. 407–420.

[27]Gruber, M., Joseph, P. F., and Azarpeyvand, M., "An experimental investigation of novel trailing edge geometries on airfoil trailing edge noise reduction," *19th AIAA/CEAS Aeroacoustics Conference*, Aeroacoustics Conferences, American Institute of Aeronautics and Astronautics, May 2013.

[28]Chase, D. M., "The character of the turbulent wall pressure spectrum at subconvective wavenumbers and a suggested comprehensive model," *Journal of Sound and Vibration*, Vol. 112, 1987, pp. 125–147.